

Machine-learning potentials for nanoscale simulations of deformation and fracture: example of TiB_2 ceramic

Shuyao Lin^{1,2*}, Luis Casillas-Trujillo², Ferenc Tasnádi², Lars Hultman², Paul H. Mayrhofer¹, Davide G. Sangiovanni², and Nikola Koutná^{1,2}

¹Technischen Universität Wien, Institute of Materials Science and Technology, Vienna, A-1060, Austria

²Linköping University, Department of Physics, Chemistry, and Biology (IFM), Linköping, SE-58183, Sweden

*shuyao.lin@tuwien.ac.at

ABSTRACT

Machine-learning interatomic potentials (MLIPs) offer a powerful avenue for simulations beyond length and timescales of *ab initio* methods. Their development for investigation of mechanical properties and fracture, however, is far from trivial since extended defects—governing plasticity and crack nucleation in most materials—are too large to be included in the training set. Using TiB_2 as a model ceramic material, we propose a strategy for fitting MLIPs suitable to simulate mechanical response of monocrystals until fracture. Our MLIP accurately reproduces *ab initio* stresses and failure mechanisms during room-temperature uniaxial tensile deformation of TiB_2 at the atomic scale ($\approx 10^3$ atoms). More realistic tensile tests (low strain rate, Poisson's contraction) at the nanoscale ($\approx 10^4$ – 10^6 atoms) require MLIP up-fitting, i.e. learning from additional *ab initio* configurations. Consequently, we elucidate trends in theoretical strength, toughness, and crack initiation patterns under different loading directions. To identify useful environments for further up-fitting, i.e., making the MLIP applicable to a wider spectrum of simulations, we assess transferability to other deformation conditions and phases not explicitly trained on.

Introduction

Simulations of materials' mechanical response—including (i) intrinsic strength and toughness, (ii) nucleation of extended defects (e.g. dislocations, stacking faults, cracks) and their implications for (iii) plasticity and fracture mechanisms^{1–3}—require length and time scales beyond limits of *ab initio* methods ($\approx 10^3$ atoms, $\ll \text{ns}$)^{4–6}. The *go-to* method in most cases would be Molecular Dynamics (MD), allowing to access atomistic pathways for deformation and fracture in nanoscale systems ($\approx 10^6$ atoms) and “realistic” operation conditions (e.g. ultra-high temperatures, times up to μs). However, a severe problem of classical MD is that the necessary interatomic potentials do not exist for most engineering materials, or, are limited in accuracy and transferability with respect to temperatures, phases, and defect structures (see e.g. Refs.^{7–9}).

A powerful avenue for MD simulations on multiple time and length scales with near *ab initio* accuracy is the application of machine learning interatomic potentials^{10–13} (MLIPs, in case of no ambiguity just “potentials”). MLIPs learn the atomic energy (or other atomic properties) as a nontrivial function of a descriptor quantifying local atomic environments in an *ab initio* training set¹⁴. Compared to conventional *ab initio* calculations, MLIPs can achieve a speed up of as much as 5 orders of magnitude^{15,16}. Previous studies showed examples of MLIPs' transferability with respect to defects (e.g. grain boundaries¹⁷, dislocation structures^{18,19}) and phases^{20,21} (e.g. Ni-Mo phase diagram illustrating superior performance of a MLIP over a classical potential²²). Recently, Tasnádi et al.²³ have demonstrated high accuracy of MLIP-predicted elastic constants for TiAlN ceramics, hence, have set the stage for

MLIP development beyond linear elastic regime.

Based on the parametrization of local structural properties, MLIPs can be fitted employing different formalisms: spectral neighbor analysis potentials (SNAP)²⁴, neural networks potentials (NNP)^{25,26}, Gaussian approximation potentials (GAP)²⁷, moment tensor potentials (MTP)²⁸, linearized interatomic potentials²⁹, or atom cluster expansion (ACE) potentials¹⁴, where only the last three are mathematically *complete*³⁰. Though some parametrizations have been formally expressed as a special case of ACE³⁰, their particular implementations may be more suitable for different training datasets and applications. Benchmarks for competing parametrizations have been published in case of carbon³¹ or graphene³², but are missing for chemically complex materials.

Besides various MLIP formalisms, additional fundamental challenges in the field are: (i) efficient training dataset generation (i.e. minimising computationally-intensive *ab initio* calculations), (ii) standardized validation procedure, and (iii) training strategies for simulations beyond *ab initio* reach. A solution to (iii) would facilitate nanoscale description of solids with atomic-scale resolution, hence, is the key to understanding differences between material's sub-micrometer and macroscopic behavior^{33–35}. Point (iii) is also a primary motivation of this study which presents methodological (MLIP development) as well as materials science discussion of nanoscale MD simulations on deformation and fracture for a model TiB_2 ceramic.

The chosen material, TiB_2 , is a widely researched representative of ultra-high temperature ceramics (UHTCs) with mature synthesis technologies^{36,37} and melting point of 3500 K³⁸.

UHTCs exhibit high hardness and resistance to oxidation, corrosion, abrasive and erosive wear^{39,40}, thus, are suitable to protect tools and machining components under extreme conditions^{41–44}. Similar to other transition metal diborides, TiB₂ crystallizes in the hexagonal A1B₂-type phase^{45–47} (α , P6/mmm) and shows outstanding mechanical properties^{48,49} including hardness of 41–53 GPa^{50–52}. From computational materials science perspective, insights into mechanical behaviour of TiB₂ and other diborides have been offered by *ab initio* calculations^{53–55} and recently also by molecular dynamics with classical empirical potentials (TiB₂^{56,57}, ZrB₂⁵⁸, HfB₂⁵⁹). To date, no MLIPs capable of predicting mechanical response of UHTCs until fracture, however, have been reported.

Here, we propose a training strategy for MLIPs suitable to model deformation and crack growth mechanisms in monocrystals from atomic to nanoscale. Viability of our approach is illustrated by MD simulations of room-temperature uniaxial tensile loading for supercells with $\approx 10^3$ – 10^6 atoms. Specifically, we use the MTP formalism and train on a small fraction (initially < 1%) of snapshots from room-temperature *ab initio* molecular dynamics (AIMD) tensile tests, iteratively expanding the training set until all configurations are reliably described. Our MLIP accurately reproduces stress evolution and failure mechanisms during tensile loading of TiB₂ at the atomic scale, but requires up-fitting for more realistic nanoscale tensile tests. Consequently, we discuss size effects in the predicted mechanical properties and fracture patterns, as well as assess MLIP’s transferability with respect to other loading conditions and phases.

Results and discussion

1 Training procedure and fitting initial MLIPs

Our general training procedure is described below (Procedure 1) and schematically depicted in Fig. 1a. Throughout this work, *ab initio* training data is generated by finite-temperature AIMD calculations generally producing many highly correlated configurationsⁱ. To avoid over-representation, our MLIP training initiates with a small fraction of AIMD configurations and exploits the MLIP’s uncertainty indication—quantified through the extrapolation/Maxvol grade⁶⁰ (γ)—to iteratively expand the training set until all AIMD configurations are reliably described. Mathematically grounded in Refs.^{60–62}, γ of a given configuration expresses how much MLIP extrapolates when predicting the corresponding energy, forces, and stresses. Specifically, $\gamma \leq 1$ means interpolation and $\gamma > 1$ extrapolation.

Note that some degree of extrapolation is acceptable. Following Shapeev and co-workers⁶³ who describe $\gamma \leq 2$ as *accurate* extrapolation, we employ a γ threshold, $\gamma_{\text{thr}} = 2$, as a condition for exiting the training loop in Procedure 1.

ⁱBy a configuration, we mean a structure labelled by *ab initio* total energy, forces acting on each ion, and six stress tensor components.

Procedure 1 MLIP training

- (1) Generate a pool of AIMD configurations.
 - (2) Divide the pool into an initial training set (TS₀), a learning set (LS), and a validation set (VS) by randomly selecting 0.5%, 79.5%, and 20% of non-overlapping configurations.
 - (3) Fit an initial MLIP (MLIP₀, trained on TS₀). If γ of all configuration in the LS and VS is below $\gamma_{\text{thr}} = 2$, exit. Else, build TS₁ by adding (maximum 15) highly extrapolative configurations from the LS to TS₀ and fit a new MLIP (MLIP₁, trained on TS₁).
 - (4) While γ of all configurations in the LS and VS is above $\gamma_{\text{thr}} = 2$, build TS_{*i*} by adding (maximum 15) highly extrapolative configurations from the LS to TS_{*i*-1}, and fit a new MLIP (MLIP_{*i*}, trained on TS_{*i*}).
-

Technical comments on Procedure 1 (for further details of MLIP training, please see the Methodology):

- MLIP₀ in the step (3) is trained from an untrained MTP. To speed-up the fitting process, MLIP_{*i*} in step (4) is fitted from MLIP_{*i*-1} if maximum γ in the (*i* – 1)th iteration is below 1000 (otherwise it is fitted from an untrained MTP).
- The VS is not used for training but only as a referenceⁱⁱ.
- Besides γ , quality of the fit at each iteration *i* in (4) is monitored through errors of energies, forces and stresses (quantified by common regression model evaluation metrics, MAE, RMSE, R², see e.g. Refs.^{64–66}) for the TS_{*i*} (fitting errors) and the VS (validation errors)ⁱⁱⁱ.

Employing Procedure 1 and the MTP formalism, we fit three MLIPs: MLIP-[0001], MLIP-[10 $\bar{1}$ 0], and MLIP-[$\bar{1}$ 2 $\bar{1}$ 0]. The training uses snapshots from room-temperature AIMD simulations for a 720-atom TiB₂ supercell, uniaxially elongated in the [0001], [10 $\bar{1}$ 0], and [$\bar{1}$ 2 $\bar{1}$ 0] crystallographic direction, respectively, with a strain step of 2% (for details of AIMD simulations, see the Methodology). The entire pool of AIMD data consists of $\approx 120,000$ configurations, where each loading condition ([0001], [10 $\bar{1}$ 0], and [$\bar{1}$ 2 $\bar{1}$ 0]) represents $\approx 1/3$ ^{iv}.

The final training sets (the last TS_{*i*} in the step (4) of Procedure 1) of MLIP-[0001], MLIP-[10 $\bar{1}$ 0], and MLIP-[$\bar{1}$ 2 $\bar{1}$ 0] contain 181, 155, and 180 configurations, respectively. The

ⁱⁱAlthough it was not the case here, the maximum γ of VS may remain high ($\gamma \gg \gamma_{\text{thr}}$) even if the maximum γ of LS is already below γ_{thr} (imagine, e.g., all configurations relevant for the description of material’s fracture ending up in the VS). Then the strategy could be switching the LS and VS, i.e. use the old VS for learning and the old LS for validation.

ⁱⁱⁱWhile not done here, one may use fitting and validation errors as additional criterion (besides γ_{thr}) for exiting the training loop.

^{iv}Since we run AIMD tensile tests until fracture, directions with higher fracture strains produce more configurations.

fitting and validation errors, quantified through the residual mean square error (RMSE), of total energies, forces, and stresses do not exceed 2.6 meV/at., 0.11 eV/Å, and 0.19 GPa, respectively.

2 MLIPs' validation against atomic scale tensile tests

As a next step, the above developed MLIPs are employed for MD calculations, from now on referred to as ML-MD. Specifically, we simulate uniaxial tensile deformation of TiB₂ with computational setup equivalent to that used in AIMD. The aim is two-fold:

- (i) To assess accuracy of quantities relevant for the targeted MLIP's application and possibly measurable in experiment. Here, key descriptors of mechanical response are (time-averaged) stresses in the loaded direction and quantities characterizing material's strength and toughness.
- (ii) To decide if MLIP up-fitting is necessary. By up-fitting we understand expanding the LS by additional *ab initio* configurations and going back to the step (4) of Procedure 1 (see Fig. 1b,c). Up-fitting is triggered when γ during a ML-MD simulation exceeds *reliable* extrapolation^v. Following Ref.⁶³ we use $\gamma_{\text{reliable}} \leq 10$ and show that such choice provides a good accuracy of stresses during atomic scale ML-MD tensile tests in relation to AIMD results.

Fig. 2a depicts stress/strain curves derived from room-temperature AIMD and ML-MD tensile tests, in which TiB₂ supercell ($\approx 10^3$ atoms, $\approx 1.5^3$ nm³) is loaded in the [0001], [10 $\bar{1}$ 0], and [$\bar{1}$ 2 $\bar{1}$ 0] direction, respectively. Note that each deformation is simulated with a MLIP trained to the respective loading condition (e.g., MLIP-[0001] for the [0001] tensile test etc.). Excellent quantitative agreement between AIMD and ML-MD results indicates reliability of our MLIPs. Specifically, (time-averaged) stresses in ML-MD differ from AIMD values by 0.07–1.94 GPa, yielding statistical errors RMSE ≈ 1.02 GPa, $R^2 \approx 0.9997$ ^{vi}. The fracture point in [0001] deformation is excluded from the analysis (there, the [0001] stress component in AIMD does not drop to zero due to long-range electrostatic effects absent in ML-MD). The extrapolation grade during all ML-MD simulations remains low ($\gamma \leq 5 < \gamma_{\text{reliable}}$), thus, suggests reliable extrapolation and does not trigger MLIP up-fitting.

^vFrom our training procedure (Procedure 1), it follows that the final MLIP yields $\gamma \leq \gamma_{\text{thr}} = 2$ for all *ab initio* configurations in the TS, VS, and LS. Finite-temperature effects, however, may cause $\gamma > \gamma_{\text{thr}}$, even during a ML-MD simulation with computational setup equivalent to that used to generate the training data (since ML-MD trajectories will not be exactly the same as those in AIMD). Then, (some of) the configurations causing $\gamma > \gamma_{\text{reliable}}$ can be simply labelled by *ab initio* energies, forces, stresses and added to the LS for up-fitting (note that this is a typical definition of *active learning*⁶⁷). At scales where direct *ab initio* calculations are unfeasible, additional configurations for up-fitting need to be generated in a different way, example of which is given in the following section.

^{vi}Note that stresses normal to the loaded direction—not vanishing due to the omission of Poisson's effect in both AIMD and ML-MD simulations—are also used for quantitative comparison.

Furthermore, we use the predicted stress/strain data to evaluate TiB₂'s (theoretical, intrinsic) tensile strength and toughness in the [0001], [10 $\bar{1}$ 0], and [$\bar{1}$ 2 $\bar{1}$ 0] direction. By tensile strength we mean the *ultimate* tensile strength, which corresponds to the global stress maximum during the tensile test and may be reached at a strain beyond the yield point⁶⁹. By tensile toughness (or toughness modulus) we understand the integrated stress/strain area until the fracture point. This property describes the ability of a material with no initial cracks to absorb mechanical energy until failure. The [$\bar{1}$ 2 $\bar{1}$ 0], [10 $\bar{1}$ 0], and [0001] tensile strength in ML-MD reaches 63.7, 55.0, and 52.7 GPa, respectively, differing from AIMD values by maximum 0.8 GPa (0.99%). The ML-MD predicted toughness along [$\bar{1}$ 2 $\bar{1}$ 0], [10 $\bar{1}$ 0], and [0001] reaches 4.3, 3.1, and 4.3 GPa, respectively, differing from AIMD values by maximum 0.029 GPa (0.67%). Note, however, that theoretical tensile strength and toughness values may be size-dependent and should saturate at large-enough supercell sizes (see nanoscale simulations in the following sections).

For MLIPs targeted to simulations of deformation and fracture, additional aspect of validation is qualitative analysis of strain-induced structural changes. This means confirming that the MLIP captures phenomena as, e.g., transformation toughening mechanisms or material's cleavage predicted by equivalent AIMD simulations. Here, our MLIPs correctly reproduce brittle failure pathways observed in AIMD of TiB₂ subject to [0001], [10 $\bar{1}$ 0], and [$\bar{1}$ 2 $\bar{1}$ 0] tensile deformation (Fig. 2b–c), as also indicated by the agreement between ML-MD and AIMD stress/strain curves (Fig. 2a). The TiB₂'s fracture strains (same in AIMD and ML-MD) are 24%, 20%, and 18% during [0001], [10 $\bar{1}$ 0], and [$\bar{1}$ 2 $\bar{1}$ 0] tensile tests, respectively.

Snapshots of the simulation cell (Fig. 2b–c) reveal formation of fracture surfaces with orientation equivalent to that in AIMD. Specifically, fracture surface for [0001] deformation almost perfectly aligns with (0001) basal planes (Fig. 2-(b-1),(c-1),d). Consistently with AIMD, ML-MD tensile loading along the [10 $\bar{1}$ 0] direction opens a void diagonally across Ti/B₂ layers (Fig. 2-(b-2),(c-2)). The fracture surface is parallel to the second order pyramidal planes of the {11 $\bar{2}$ 2} family (Fig. 2d). For the [$\bar{1}$ 2 $\bar{1}$ 0] loading condition, fracture planes are approximately parallel to the {10 $\bar{1}$ 0} prismatic planes (Fig. 2-(b-3),(c-3),d).

3 MLIPs' up-fitting for nanoscale tensile tests

MLIP-[0001], MLIP-[10 $\bar{1}$ 0], and MLIP- $[\bar{1}2\bar{1}0]$ provide reliable description of TiB₂'s response to uniaxial tensile loading at the atomic scale. This is indicated by low extrapolation grades ($\gamma \leq 5 < \gamma_{\text{reliable}}$) as well as accuracy of stress/strain curves, theoretical strength and toughness, and fracture mechanisms consistent with AIMD observations (see previous section).

As a next step, we simulate more realistic tensile tests at the nanoscale, including Poisson's contraction and continuously increasing the applied strain. For clarity, we establish the following notation.

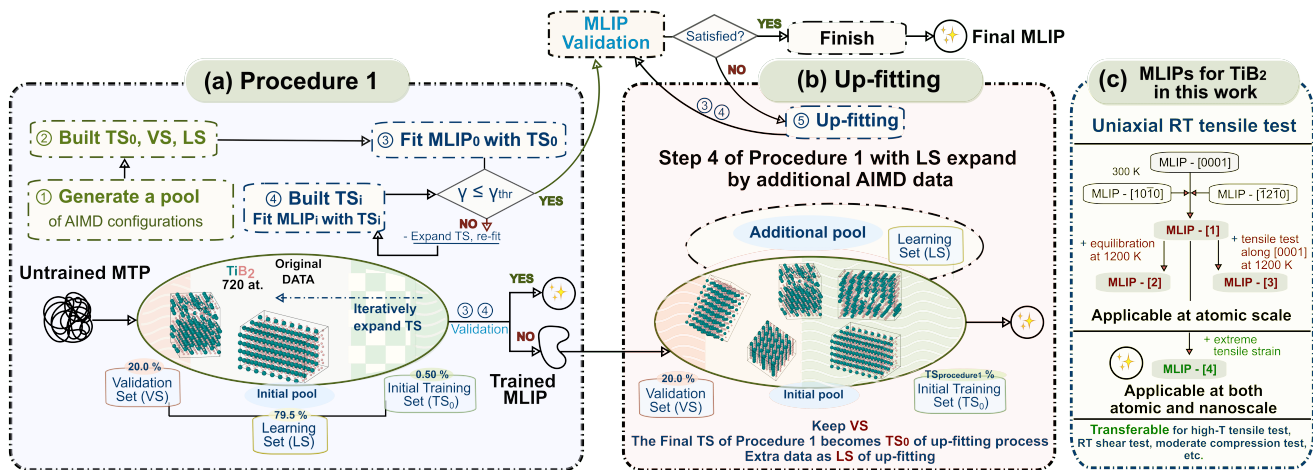


Figure 1. Schematic visualization of (a) our general training procedure (Procedure 1, Section 1), and (b) up-fitting (Section 2, 3). (c) Relationships between MLIPs developed in this work (Section 1, 2, and 3) showing how MLIP-[4] was produced by up-fitting, starting from MLIP-[0001].

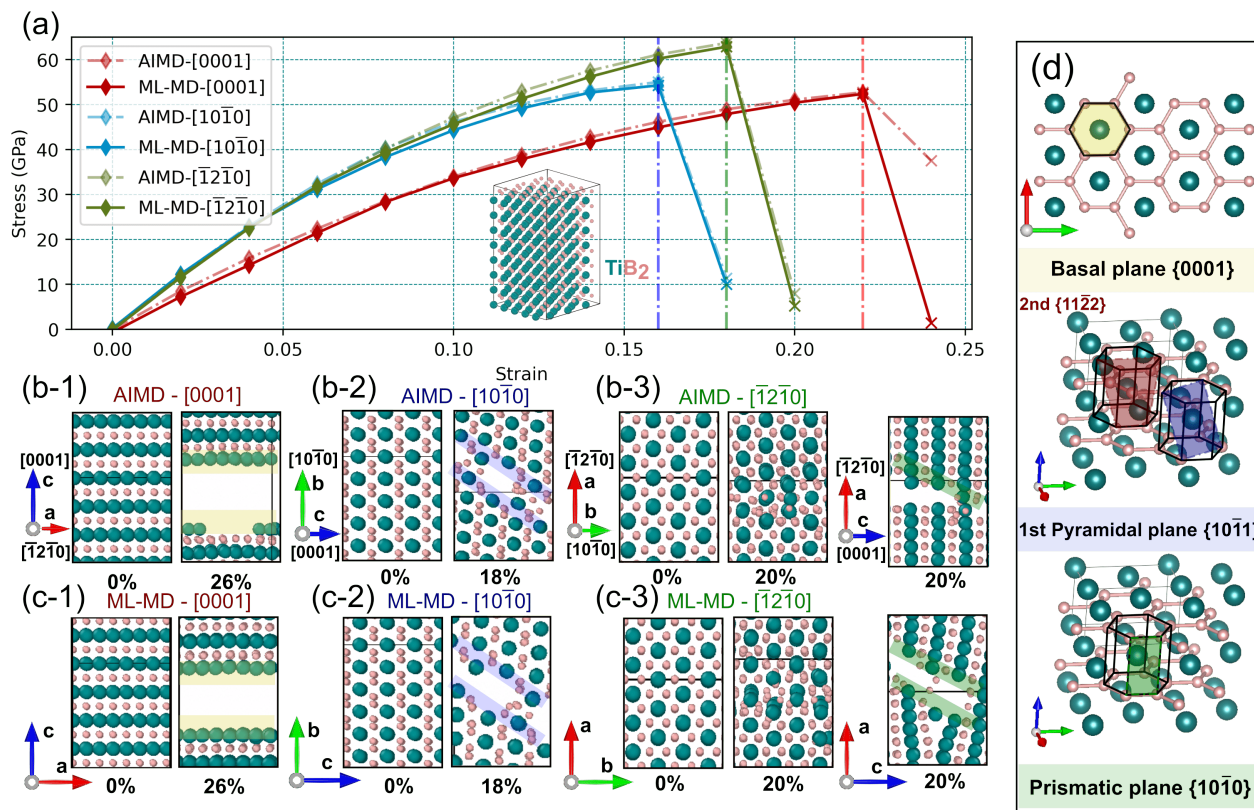


Figure 2. Validation of the here-developed MLIPs (MLIP-[0001], MLIP-[1010], and MLIP-[1210]). (a) Comparison of AIMD and ML-MD stress/strain curves for TiB₂ subject to [0001], [1010], and [1210] tensile deformation at 300 K, using a 720-atom supercell with dimensions of $\approx (1.52 \times 1.58 \times 2.57) \text{ nm}^3$. Only the stress component in the loaded direction is plotted. (b, c) Snapshots of the fracture point in AIMD (b-1, b-2, b-3) and ML-MD (c-1, c-2, c-3). (d) Terminology used for fracture surfaces (following Ref.⁶⁸).

- **Atomic scale tensile tests** (presented in the previous section) are uniaxial tensile tests with the following setup:

- (i) Supercells with $\approx 10^3$ atoms. Specifically, our supercell has 720 atoms, corresponding to dimensions of $\approx (1.5 \times 1.6 \times 2.6) \text{ nm}^3$.
- (ii) A 2% strain step with a 3 ps equilibration under fixed lattice vectors normal to the loaded direction (i.e. no Poisson’s contraction).

- **Nanoscale tensile tests** are uniaxial tensile tests with the following setup:

- (i) Supercells with 10^4 – 10^6 atoms. Specifically, we use four supercells: $S1$ (12,960 at.), $S2$ (141,120 at.), $S3$ (230,400 at.), and $S4$ (432,000 at.), where $S1 \approx 5^3 \text{ nm}^3$ and $S4 \approx 15^3 \text{ nm}^3$.
- (ii) Continuous deformation (strain rate 50 \AA/s) and relaxation of lattice vectors normal to the loaded direction (i.e. including Poisson’s contraction).

Employing MLIP-[0001], MLIP-[10 $\bar{1}$ 0], and MLIP-[$\bar{1}$ 2 $\bar{1}$ 0] for room-temperature nanoscale tensile tests results in unphysical dynamics (losing atoms) and rapidly increasing extrapolation grades ($\gamma \gg 10^3 \gg \gamma_{\text{reliable}}$) when approaching the fracture point. This indicates we have reached length scales where extended defects—absent in atomic scale simulations—dominate materials’ deformation. To enable description of TiB₂’s fracture at the nanoscale, our MLIPs require up-fitting (recall Fig. 1b). Generally, this is a very non-trivial task^{70,71}, since structures causing large γ cannot be directly treated by *ab initio* calculations^{vii}.

Below we describe up-fitting steps leading to MLIP-[4] (schematically depicted in Fig. 1c), which is a MLIP enabling room-temperature nanoscale tensile tests for TiB₂.

- We produce MLIP-[1] by up-fitting MLIP-[0001], where the LS is expanded by final TSs of MLIP-[10 $\bar{1}$ 0] and MLIP-[$\bar{1}$ 2 $\bar{1}$ 0]^{viii}. Although MLIP-[1] does not yet suffice to describe TiB₂’s fracture during tensile deformation at the nanoscale ($\gamma \gg \gamma_{\text{reliable}}$), it can be applied to simulate atomic scale tensile tests for all the three loading directions.

In particular, MLIP-[1] yields low extrapolation grades ($\gamma \leq 6 < \gamma_{\text{reliable}}$) and correctly reproduces fracture mechanisms from AIMD. MLIP-[1] also preserves nearly the same accuracy as MLIP-[0001], MLIP-[10 $\bar{1}$ 0], and

^{vii}Due to the fact that direct *ab initio* calculations are unfeasible at the nanoscale, proving that a MLIP predicts the “correct physics” is possible only through indirect indications. These include the MLIP’s uncertainty indication, γ , and calculations of properties that can be derived also from atomic scale simulations, e.g. lattice parameters or theoretical tensile strength.

^{viii}Fitting errors (RMSEs) of energies, forces, and stresses do not exceed 3.7 meV/at., 0.12 eV/ \AA , and 0.25 GPa, respectively. Extrapolation grades of all *ab initio* configurations produced so are below $\gamma_{\text{thr}} = 2$. The final TS has 151 (720-atom) TiB₂ configurations, which is less than the individual TSs of MLIP-[0001], MLIP-[10 $\bar{1}$ 0], and MLIP-[$\bar{1}$ 2 $\bar{1}$ 0] combined.

MLIP-[$\bar{1}$ 2 $\bar{1}$ 0]^{ix}. In terms of (time-averaged) stresses, differences from AIMD values, are 0.13–1.47 GPa, resulting in statistical errors $\text{RMSE} \approx 0.79 \text{ GPa}$, $R^2 \approx 0.9999$. The corresponding stress/strain curves are presented in the Suppl. Mat. (Fig. S2). Additionally, MLIP-[1] provides good accuracy of room-temperature elastic constants, C_{ij} (Tab. 1), differing from AIMD-calculated values by less than 4.9%. Although our MLIPs are not targeted to accurate predictions of C_{ij} ^x due to low energy cutoff used in the underlying AIMD training set, the here obtained values further underpin reliability of MLIP-[1]^{xi}.

- We up-fit MLIP-[1] using three different LSs, producing MLIP-[2], MLIP-[3], and MLIP-[4]. Specifically, MLIP-[2] and MLIP-[3] learn from AIMD snapshots of TiB₂ equilibrated at 1200 K (MLIP-[2]), and sequentially elongated in the [0001] direction until cleavage (MLIP-[3]). MLIP-[4] learns from AIMD snapshots of TiB₂ elongated by 150% in the [0001] direction, initializing atoms at ideal lattice sites and equilibrating at 300 and 1200 K under fixed volume and shape^{xii}. Such large strain quickly induces fracture, thus providing additional information for training MLIP on highly deformed lattice environments and surface properties.

MLIP-[2], MLIP-[3], and MLIP-[4] all provide reliable description of room-temperature tensile tests at the atomic scale ($\gamma \leq 5 < \gamma_{\text{reliable}}$). The corresponding stress/strain curves nearly overlap with AIMD-calculated ones (Supp. Mat. Fig. S2) and also fracture mechanisms are correctly reproduced. The accuracy of elastic constants remains the same as for MLIP-[1]. At the nanoscale, MLIP-[2] and MLIP-[3] exhibit lower γ than those obtained by MLIP-[1]. However, the sought improvement ($\gamma \leq \gamma_{\text{reliable}}$) is achieved only by MLIP-[4], which will be used to carry out nanoscale ML-MD simulations of TiB₂ deformation.

Besides reliability indication through γ , MLIP-[4] provides physically sound stress/strain curves and dynamics of nanoscale tensile deformation (illustrated in Supp. Mat. Fig. S4, and in the following section). Additional indication of MLIP-[4]’s reliability are lattice parameters evaluated by equilibrating atomic scale ($\approx 10^3$ atoms)

^{ix}Generally, this does not have to be the case. Making a MLIP applicable to a wider spectrum of environments (here, MLIP-[1] can tackle all the three loading conditions) may lead to decreased accuracy for a particular simulation (here, e.g., MLIP-[10 $\bar{1}$ 0] may be in principle more accurate in describing the [10 $\bar{1}$ 0] loading condition).

^xA training approach suitable for accurate predictions of C_{ij} has been recently suggested by Ref.²³.

^{xi}Furthermore, the only computational report of TiB₂’s elastic constants at finite temperatures, besides ours, is Ref.⁷², which does not use AIMD but a method based on *ab initio* calculations of C_{ij} at 0 K and *ab initio* phonon theory of thermal expansion.

^{xii}Note that all the three LSs are generated at low computational and human time. In particular, we do not “hand-design” any material-specific environments or e.g. surfaces, only pull a TiB₂ supercell (720-atoms, equilibrated at 300 K and 1200 K) along one of the three lattice vectors.

Table 1. Elastic constants, C_{ij} (in GPa), of TiB_2 (at temperature T (K))—calculated using the here-developed MLIP (MLIP-[1])—together with the polycrystalline bulk modulus, B (in GPa), shear modulus, G (in GPa), Young’s modulus, E (in GPa), and Poisson’s ratio, ν , compared to reference *ab initio* and experimental (exp.) data. Ref.⁷³ and Ref.⁷⁴ is for TiB_2 single and polycrystal, respectively. AIMD and ML-MD elastic constants were evaluated following Ref.⁷⁵, based on a second-order polynomial fit of the [0001], [10 $\bar{1}$ 0], and [$\bar{1}$ 2 $\bar{1}$ 0] stress/strain data (C_{11} , C_{12} , C_{13} , C_{33}) and of the (0001)[$\bar{1}$ 2 $\bar{1}$ 0], (10 $\bar{1}$ 0)[$\bar{1}$ 2 $\bar{1}$ 0], and (10 $\bar{1}$ 0)[0001] shear stress/strain data (C_{44}), assuming strains up to 4%. For details see the Methodology section.

	Nr. of atoms	T	C_{11}	C_{33}	C_{44}	C_{12}	C_{13}	E	B	G	ν	Source
DFT	3	0	655	461	260	65	99	582	253	266	0.110	Ref. ⁷⁶
DFT	12	0	654	464	259	76	115	591	263	263	0.125	This work
AIMD	720	300	588	430	252	79	111	547	244	243	0.126	This work
ML-MD	720	300	588	409	261	85	98	554	236	246	0.113	This work
Exp.	-	300	660	432	260	48	93	565	244	266	0.099	Ref. ⁷³
Exp.	-	300	588	503	238	72	84	575	249	255	0.114	Ref. ⁷⁴

and nanoscale ($\approx 10^4$ – 10^6 atoms) TiB_2 supercells. As shown in Tab. 2, the values do not differ by more than 0.01%.

Table 2. Lattice constants, a and c (in Å), of TiB_2 at temperature $T = \{0, 300, 1200\}$ K calculated using the here-developed ML potential (MLIP-[4]), compared to reference *ab initio* and experimental (exp.) values (Ref.⁷⁷ and Refs.^{78,79} are for TiB_2 powder and thin films, respectively).

	Nr. of atoms	T	a	c	Source
DFT	3	0	3.038	3.234	Ref. ⁷⁶
DFT	12	0	3.033	3.227	This work
AIMD	720	300	3.035	3.218	This work
ML-MD	720	300	3.036	3.218	This work
ML-MD	$(13\text{--}430)\cdot 10^3$	300	3.036	3.217	This work
Exp.	-	300	3.032	3.229	Ref. ⁷⁷
Exp.	-	300	3.029	3.229	Ref. ⁷⁸
Exp.	-	300	3.021	3.230	Ref. ⁷⁹
AIMD	720	1200	3.056	3.249	This work
ML-MD	720	1200	3.056	3.249	This work
ML-MD	$(13\text{--}430)\cdot 10^3$	1200	3.047	3.239	This work

To offer some understanding of why MLIP-[4] enables nanoscale tensile tests, one needs to analyse the corresponding training set, TS(MLIP-[4]). In Fig. 3, we visualize selected characteristics of TS(MLIP-[4]) in comparison to the training set of MLIP-[1], TS(MLIP-[1]), where the latter is not applicable to simulate TiB_2 ’s fracture at the nanoscale. The radial distribution function (RDF, Fig. 3a) and bond angle distribution analysis (Suppl. Mat., Fig.S6) suggest minor geometrical differences between structures contained in TS(MLIP-[1]) and TS(MLIP-[4]). Their total energy and stress distribution, however, differ significantly (Fig. 3b). In particular, TS(MLIP-[4]) contains atomic configurations with higher total energy and higher total energy in combination with higher stress in principal crystallographic axes, which are missing in TS(MLIP-[1]). An illustration of structures from the two training sets is given in Fig. 3c. The chosen snapshots indicate that TS(MLIP-[4]) provides a variety of atomic environments relevant for simulations of non-stoichiometry, locally amorphous regions, and surfaces, which are likely to be helpful also for simulations of extended defects nucleating due to high strains during tensile tests.

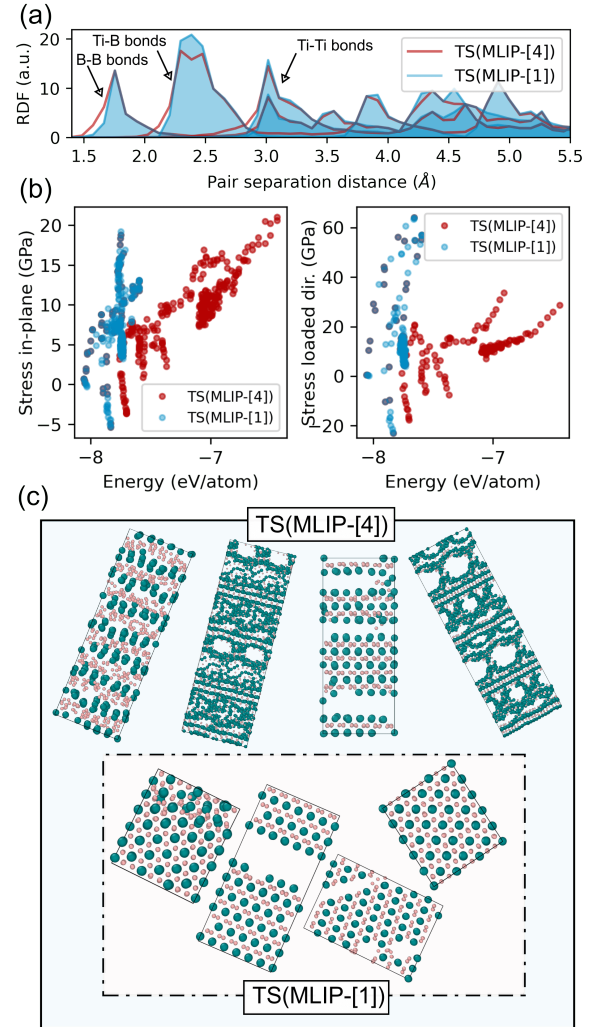


Figure 3. Qualitative differences between training sets (TSs) of the here-developed ML potentials (MLIP-[1], MLIP-[4]). Only MLIP-[4] is suitable for nanoscale ML-MD tensile tests. (a) Radial distribution function (RDF, with 5.5 Å cutoff) for B–B, Ti–B, and Ti–Ti bonds (integrated over all configurations). (b) Stress components (in-plane and in the loaded direction) vs. total energy of all configurations in the training set. (c) Snapshots of representative structures from the two training sets.

4 Size effects in tensile response of TiB₂

Equipped with the above developed MLIP-[4], in this section we discuss TiB₂'s response to room-temperature uniaxial tensile loading from atomic to nanoscale. Recall that an important difference between our atomic and nanoscale tensile tests is that the former disregard Poisson's contraction. The stress/strain curves calculated at room temperature are depicted in Fig. 4. For strains below $\approx 10\%$, stresses for the respective loading direction ([0001], [10 $\bar{1}$ 0], and [$\bar{1}$ 2 $\bar{1}$ 0]) almost perfectly overlap regardless the supercell size ($\approx 10^3$ – 10^6 atoms). Such overlap indicates consistency in elastic constants derived from atomic and nanoscale models^{xiii}. Furthermore, also elastic isotropy of the basal plane is size independent. The isotropy is suggested by nearly the same initial slope of stress/strain curves for [$\bar{1}$ 2 $\bar{1}$ 0] and [10 $\bar{1}$ 0] elongation and in line with experimental reports for hexagonal crystals⁸⁰.

Due to Poisson contraction, however, differences in stress/strain curves emerge beyond the linear-elastic regime. A shrinkage of the lattice parameters normal to the applied tensile strain yields Poisson's ratio ($\nu \approx 0.127$ ^{xiv}) consistent with the value obtained from elastic constants ($\nu \approx 0.113$, see Tab. 1), thus underpinning reliability of MLIP-[4]. Approaching the fracture point, differences between TiB₂'s tensile behavior at atomic and nanoscale become more apparent^{xv}. These can be illustrated by ideal strengths and toughness moduli (Tab. 3). Although theoretical strength and toughness exhibit qualitative differences in their directional dependence at the atomic scale and nanoscale, these properties are well saturated for all nanoscale supercells (S1–S4). Specifically, the [$\bar{1}$ 2 $\bar{1}$ 0] direction exhibits the highest tensile strength (≈ 56 GPa), followed by the [0001] direction (≈ 54 GPa), and the [10 $\bar{1}$ 0] direction (≈ 51 GPa)^{xvi}. For comparison, the hardness reported for TiB₂ thin films, typically [0001]-textured, is 41–53 GPa^{50–52}. The [0001] direction exhibits the highest toughness modulus (≈ 4.80 GPa), followed by the [$\bar{1}$ 2 $\bar{1}$ 0] direction (≈ 3.37 GPa), and the [10 $\bar{1}$ 0] direction (≈ 2.78 GPa)^{xvii}.

Besides characterizing directional dependence of tensile strength and toughness in dislocation-free monocrystals, nanoscale simulations also provide insights into crack nucleation and growth mechanisms. This can be illustrated—and contrasted with atomic scale ML-MD—using the example of

^{xiii}Note that in order to obtain the C_{44} elastic constant, we would need to perform additional shear simulations, which we did only at the atomic scale (recall Tab. 1).

^{xiv}The Poisson contraction was calculated as $\nu = -\frac{d\epsilon_{\text{compressed}}}{d\epsilon_{\text{elongated}}}$, where the $d\epsilon_{\text{compressed}}$ ($d\epsilon_{\text{elongated}}$) is the lattice parameter shrinkage (increment) orthogonal (parallel) to the loading direction. The presented value is an average of Poisson's ratios for both in-plane directions.

^{xv}Even more significant size effects may be expected for materials with strain-activated plasticity mechanisms.

^{xvi}At the atomic scale, in contrast, TiB₂'s tensile strength is the highest in the [$\bar{1}$ 2 $\bar{1}$ 0] direction (≈ 64 GPa), followed by [10 $\bar{1}$ 0] (≈ 55 GPa) and [0001] (≈ 53 GPa).

^{xvii}Atomic-scale ML-MD indicates nearly the same [0001] and [$\bar{1}$ 2 $\bar{1}$ 0] tensile toughness (≈ 4.32 GPa) which is above that reached during the [10 $\bar{1}$ 0] tensile test (≈ 3.11 GPa).

[0001] tensile test (Fig. 5). At the atomic scale, all atoms in TiB₂ vibrate close to their ideal lattice sites until a sudden brittle cleavage induces formation of two surfaces almost perfectly parallel with (0001) basal planes (Fig. 5, row 1). At the nanoscale, fracture is initiated by opening of voids accompanied by local necking which produces lattice re-orientations (Fig. 5, row 2 and 3). Rapid void coalescence and fraying of ligaments results in corrugated fractured surfaces, predominantly with (0001) orientation. Following the stress release, inner parts of the crystal relax back to the ideal TiB₂ lattice sites.

The S1 supercell yields in only one region (Fig. 5, row 2). The larger S2, S3, and S4 supercells—where only S4 is depicted in Fig. 5—do not fracture in two pieces but show few-nm-size cracks inside. Here, fracture surfaces do not align only with the basal planes but also with the {10 $\bar{1}$ 1} first order pyramidal planes (recall the notation in Fig. 2d). Volumetric strain analysis (Fig. 5d,e) highlights locally increased tensile strain concentration surrounding small voids (see TiB₂ slice at $\approx 27\%$ strain) due to decreased interplanar spacings between Ti and B layers (predominantly due to [0001] compression) above and below the voids. The largest S4 supercell allows for crack propagation under different directions, thus, provides a certain statistical viewpoint missing in the S1 supercell and at the atomic scale.

For the [10 $\bar{1}$ 0] tensile test, size effects in fracture mechanisms are compared in Fig. 6. At the atomic scale, two voids open diagonally across Ti/B layers (Fig. 6, row 1). At the nanoscale, we observe nucleation of V-shaped cracks, as illustrated for the S1 and the S4 supercell (Fig. 6, row 2 and 3, and panels c, d), where S4 additionally reveals lattice rotation near the V-shaped defects. We infer that loading in the direction of strong covalent B–B bonds most often induces crack deflection and fracture at {1122} family of surfaces parallel to the second order pyramidal planes.

Changing to the [$\bar{1}$ 2 $\bar{1}$ 0] tensile deformation, atomic scale simulations predict fracture along {10 $\bar{1}$ 0} prismatic planes (Fig. 7, row 1). This is underpinned also by nanoscale ML-MD (Fig. 7, row 2 and 3), suggesting that crack growth is most often orthogonally and diagonally across Ti/B layers (see the dashed line with arrow in Fig. 7e).

5 Other loading conditions and MLIP's transferability

Targeted applications of our MLIP (MLIP-[4]) are atomic to nanoscale simulations of TiB₂ subject to room-temperature uniaxial tensile loading. Although the training set only contained snapshots of a 720-atom TiB₂ supercell, with one of the three lattice vectors elongated with respect to the equilibrium length at 300 K, Fig. 3c indicates variety of atomic environments relevant for simulations of non-stoichiometry, locally amorphous regions, or e.g. surfaces.

Here we discuss transferability of our MLIP to simulations for which it has not been explicitly trained. Accuracy of the predicted observables (e.g. shear strengths or surface energies) is presented in the context of extrapolations grades, allowing

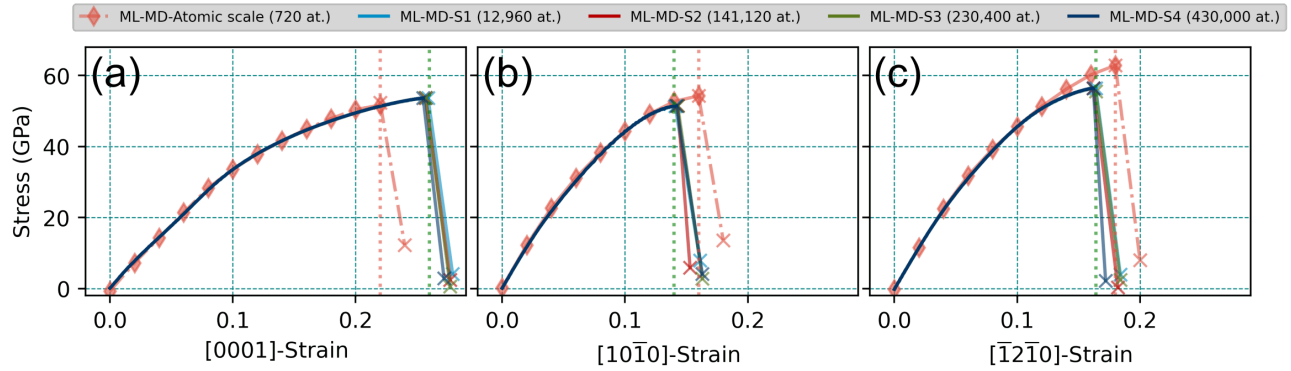


Figure 4. ML-MD stress/strain curves (obtained by MLIP-[4]) for TiB_2 subject to (a) $[0001]$, (b) $[10\bar{1}0]$, and (c) $[\bar{1}2\bar{1}0]$ tensile deformation at 300 K. Only the stress component in the loaded direction is plotted. The orange diamonds correspond to atomic scale ML-MD simulations, while the solid lines correspond to nanoscale ML-MD simulations, as defined at the beginning of this section.

Table 3. Mechanical properties of various TiB_2 supercells derived from room-temperature ML-MD stress/strain data (Fig. 4) together with 1200 K results for comparison.

Nr. of atoms	T (K)	Dimensions (nm)			Strength (GPa)			Toughness (GPa)			Fracture strain (%)		
		<i>a</i>	<i>b</i>	<i>c</i>	$[0001]$	$[10\bar{1}0]$	$[\bar{1}2\bar{1}0]$	$[0001]$	$[10\bar{1}0]$	$[\bar{1}2\bar{1}0]$	$[0001]$	$[10\bar{1}0]$	$[\bar{1}2\bar{1}0]$
720	300	1.51	1.58	2.57	52.72	55.01	63.69	4.33	3.11	4.32	22.0	16.0	18.0
12,960 (S1)	300	4.55	4.73	5.15	53.71	51.36	56.40	4.83	2.77	3.38	26.4	14.3	16.8
141,120 (S2)	300	10.63	11.05	10.30	53.69	51.43	56.41	4.81	2.78	3.37	26.4	14.3	16.8
230,400 (S3)	300	12.14	12.63	12.87	53.71	51.43	56.39	4.82	2.78	3.37	26.3	14.3	16.8
432,000 (S4)	300	15.18	15.79	15.45	53.64	51.47	56.42	4.80	2.78	3.37	26.2	14.2	16.8
720	1200	1.53	1.59	2.60	43.87	45.21	51.35	3.27	2.29	3.07	20.0	16.0	16.0
432,000 (S4)	1200	15.26	15.86	15.52	43.27	41.31	44.72	3.45	1.96	2.32	21.6	12.8	14.1

to identify types of configurations beneficial for further up-fitting, thus, broadening the MLIP’s applicability.

- **High-temperature tensile deformation of TiB_2 .** Since TiB_2 is a UHTCs (see the Introduction), modelling its mechanical behaviour at extreme temperatures is of high practical relevance. Here we choose 1200 K which is close to the highest anti-oxidation temperature of Ti reported experimentally⁸¹.

Atomic scale $[0001]$, $[10\bar{1}0]$, and $[\bar{1}2\bar{1}0]$ tensile tests at 1200 K show excellent quantitative agreement with AIMD simulations at the same temperature (see Suppl. Mat., Fig. S5). Specifically, differences from AIMD-calculated stresses are 0.01–3.54 GPa, resulting in statistical errors $\text{RMSE} \approx 1.85$ GPa, $R^2 \approx 0.9997$. Extrapolations grades indicate reliable extrapolation ($\gamma \leq 7 < \gamma_{\text{reliable}}$).

TiB_2 ’s theoretical tensile strength at 1200 K decreases by about 17–19% compared to 300 K. For tensile toughness, our simulations predict $\approx 25\%$ decrease. Fracture mechanisms remain qualitatively unchanged with respect to 300 K.

- **Room-temperature shear deformation of TiB_2 .** Simulations of shear deformation provide useful insights for understanding of how dislocations nucleate and move in generally brittle UHTCs^{82,83}. Furthermore, as diborides

typically crystallize in layered structures (α , γ , ω) which can be viewed as different stackings of the transition metal planes, shearing may also induce transformation toughening⁸⁴. Following Ref.⁵⁵, we choose to simulate the $(0001)[\bar{1}2\bar{1}0]$, $(10\bar{1}0)[\bar{1}2\bar{1}0]$, and $(10\bar{1}0)[0001]$ shear deformation^{xviii}.

Stress evolution during atomic scale shear deformation (Fig. 8a) agrees well with equivalent AIMD simulations. This is particularly the case for strains below $\approx 20\%$, where stresses differ from AIMD values by 0.01–5.08 GPa (yielding statistical errors $\text{RMSE} \approx 3.72$ GPa, $R^2 \approx 0.9993$) and γ is close to reliable extrapolation ($\gamma < 14$). Considering that the training set did not contain any sheared supercells, this is a plausible result. Shear strains above $\approx 20\%$ induce notably larger discrepancies in stresses (differing from AIMD by 5.36–8.51 GPa) and increased γ ($\gamma \leq 26$). The main reason is that lattice slip—responsible for (partial) stress release subject to shearing—does not occur exactly at the same strain step, although the mechanism is identical (Fig. 8b–d)^{xix}.

The predicted shear strengths (49, 57, and 51 GPa for the $(0001)[\bar{1}2\bar{1}0]$, $(10\bar{1}0)[\bar{1}2\bar{1}0]$, and $(10\bar{1}0)[0001]$ de-

^{xviii}There are various slip systems experimentally observed in diborides depending on temperature. For an overview, please see Ref.⁸⁰.

^{xix}Note that if repeated many times, AIMD shear simulations would not exhibit lattice slip exactly at the same strain step either.

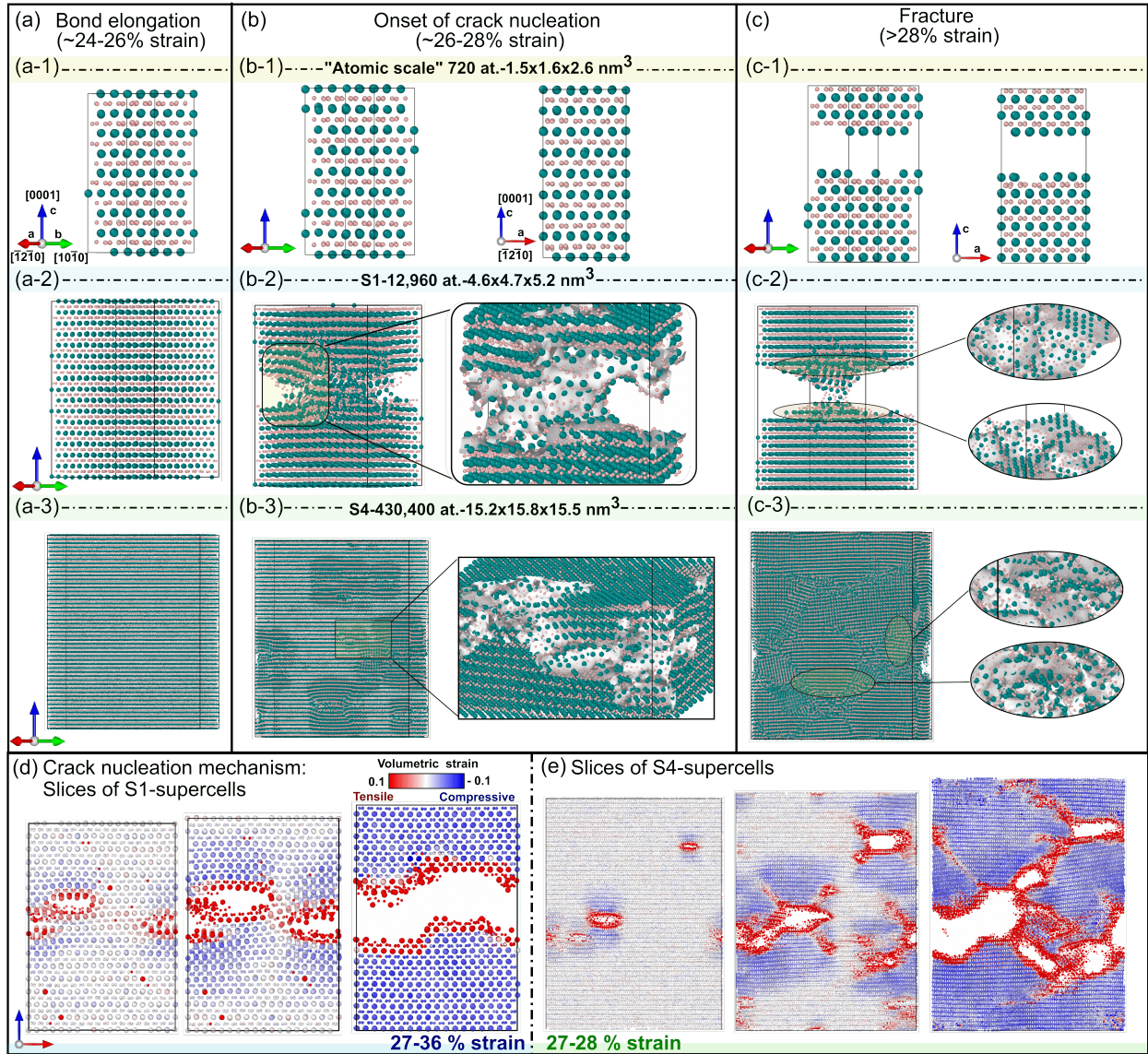


Figure 5. Illustration of size effects in (room-temperature) ML-MD [0001] tensile tests for TiB_2 at key deformation stages: (a) **bond elongation** in the loaded direction, (b) **onset of crack nucleation**, and (c) **fracture**. Thin slices of the nanoscale (d) S1 and (e) S4 supercells color-coded based on volumetric strain (using the corresponding equilibrium structure as reference). Red (blue) regions denote high tensile (compressive) strain.

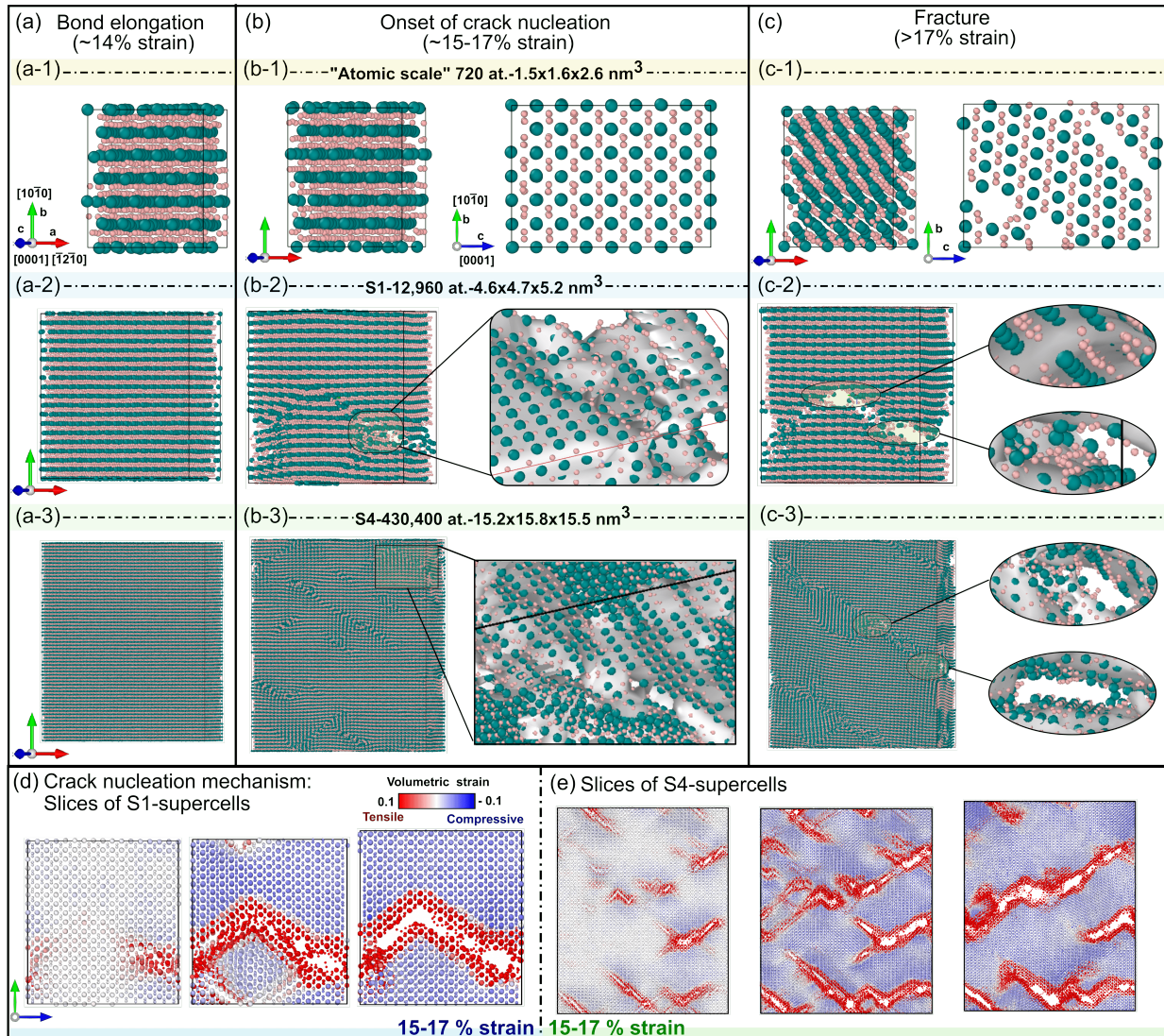


Figure 6. Illustration of size effects in (room-temperature) ML-MD $[10\bar{1}0]$ tensile tests for TiB_2 at key deformation stages: (a) **bond elongation** in the loaded direction, (b) **onset of crack nucleation**, and (c) **fracture**. Thin slices of the nanoscale (d) S1 and (e) S4 supercells color-coded based on volumetric strain (using the corresponding equilibrium structure as reference). Red (blue) regions denote high tensile (compressive) strain.

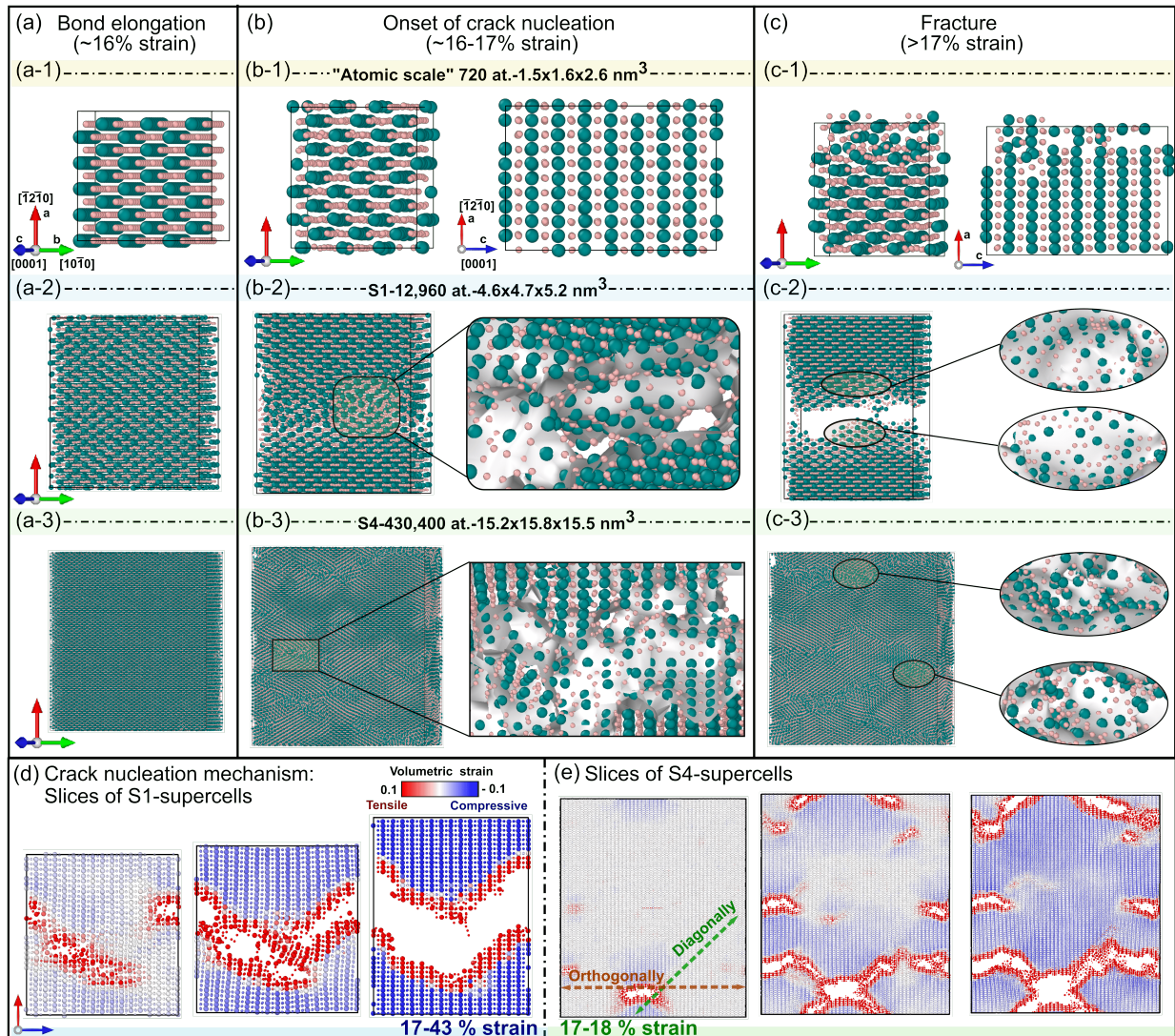


Figure 7. Illustration of size effects in (room-temperature) ML-MD $[\bar{1}2\bar{1}0]$ tensile tests for TiB_2 at key deformation stages: (a) **bond elongation** in the loaded direction, (b) **onset of crack nucleation**, and (c) **fracture**. Thin slices of the nanoscale (d) S1 and (e) S4 supercells color-coded based on volumetric strain (using the corresponding equilibrium structure as reference). Red (blue) regions denote high tensile (compressive) strain.

formation, respectively) are $\approx 8\%$ below AIMD values (58, 72, and 68 GPa). Shear-induced structural changes correctly reproduce AIMD observations. Specifically, a basal plane slip is activated subject to $\approx 24\%$ (0001)[$\bar{1}2\bar{1}0$] shear strain, restoring nearly ideal TiB_2 lattice sites (Fig. 8b). The (10 $\bar{1}0$)[$\bar{1}2\bar{1}0$] shear (Fig. 8c) induces plastic deformation, first via ($\bar{1}2\bar{1}0$)[10 $\bar{1}0$] slip, which occurs at $\approx 30\%$, and then via (10 $\bar{1}0$)[$\bar{1}2\bar{1}0$] slip at $\approx 50\%$ strain. Both mechanisms are accompanied by displacements of Ti and B atoms from the ideal TiB_2 lattice sites^{xx}. The (10 $\bar{1}0$)[0001] shear (Fig. 8d) causes slipping along the (tilted) [10 $\bar{1}0$] direction ($\approx 26\%$ strain) and the [0001] direction ($\approx 50\%$ strain), where the latter results in significant displacements of B atoms.

Overall, we infer that MLIP up-fitting would benefit from severely sheared configurations. Already the current potential (MLIP-[4]), nonetheless, suffices to estimate shear strengths and stress release mechanisms at the atomic scale.

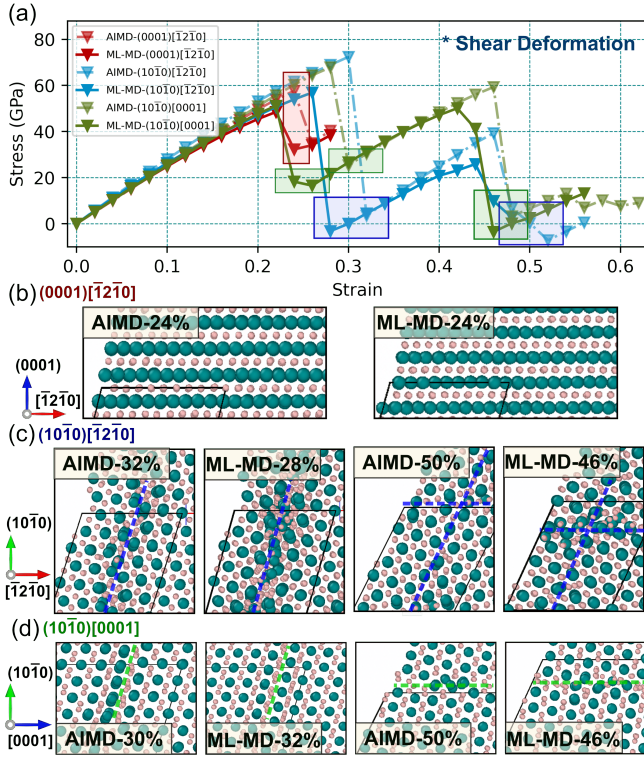


Figure 8. Transferability of the here-developed MLIP (MLIP-[4]) to atomic scale simulations of room-temperature shear deformation. (a) Comparison of AIMD and ML-MD stress/strain curves for TiB_2 subject to (0001)[$\bar{1}2\bar{1}0$], (10 $\bar{1}0$)[$\bar{1}2\bar{1}0$], and (10 $\bar{1}0$)[0001] shear. (b, c, d) Selected snapshots at strain steps marked by shaded rectangles in (a). The dashed lines guide the eye for the slip direction described in the text.

^{xx}The phenomenon may be rationalized by high energetic costs of slip in the (tilted) [$\bar{1}2\bar{1}0$] direction, which would require breaking strong covalent B–B bonds.

- **Room-temperature volumetric compression of TiB_2 .** Training on snapshots of compressed structures may be important not only in obvious cases, such as e.g. simulations of uniaxial compression or nanoindentation, but also in order to correctly account for Poisson’s contraction during tensile deformation. For TiB_2 , the relatively low Poisson’s ratio (Tab. 1) induces rather small compression, accurately reproduced by MLIP-[4] at the nanoscale^{xxi}. Here we simulate severe (room-temperature) volumetric compression—shrinking *all* lattice vectors by up to 12%—to illustrate rapidly growing γ and how this can be improved by up-fitting.

As shown in Fig. 9, compression-induced stresses along main crystallographic directions are indeed *extreme*. In AIMD, they exceed 50 GPa for a 5% compression and reach ≈ 150 GPa for a 10% compression. Our MLIP yields satisfactory agreement with AIMD for volumetric compression of 1–2%, with stress tensor components differing from *ab initio* values by less than 1.83 GPa (9.57%) and γ indicating reliable extrapolation ($\gamma \leq 10 = \gamma_{\text{reliable}}$). Further compression (of each lattice vector) up to 10%, however, causes increasing deviations from AIMD stresses and $\gamma \approx 10^2\text{--}10^3$.

We illustrate the effect of up-fitting by producing a new MLIP (MLIP-[4]_{plus}) which learns from AIMD snapshots of a 10% volumetrically-compressed TiB_2 (added to the LS of MLIP-[4]). This not only greatly improves accuracy for the 10% compression—stress differences are maximum 0.79 GPa (0.48%) and $\gamma \leq 2$ —but also within the entire compression range (see red data points in Fig. 9).

- **Surface energies of TiB_2 .** Surfaces are undoubtedly relevant for simulations of fracture. For routine MLIP development, however, it is desirable to minimize human time handcrafting material-specific surfaces. The here-suggested training data generation is easily automated and may already include atomic environments relevant for calculations of low-energy surfaces (recall Fig. 2c).

Methodologically, calculations of finite-temperature surface energies, E_{surf} , are a non-trivial task. We stick to a simple 0 K calculation of stoichiometric (1:2 Ti-to-B) surfaces via molecular statics (MS). The E_{surf} values predicted by ML-MD differ from *ab initio* calculations by 0.03 J/m² (1.40%) for $E_{\text{surf}}(0001)$, 0.04 J/m² (1.68%) for $E_{\text{surf}}(\bar{1}2\bar{1}0)$, and 0.13 J/m² (5.75%) for $E_{\text{surf}}(10\bar{1}0)$. This is a very good agreement, underlined also by low extrapolation grades ($\gamma \leq 12$)^{xxii}.

^{xxi}Specifically, Poisson’s ratio derived from lattice parameter shrinkage during nanoscale tensile tests quantitatively agrees with that calculated from AIMD elastic constants (Tab. 1).

^{xxii}For accurate surface energy calculations, however, relevant surface structures should be explicitly trained on using accurate-enough *ab initio* dataset (in contrast to our philosophy of large but less accurate training configurations).

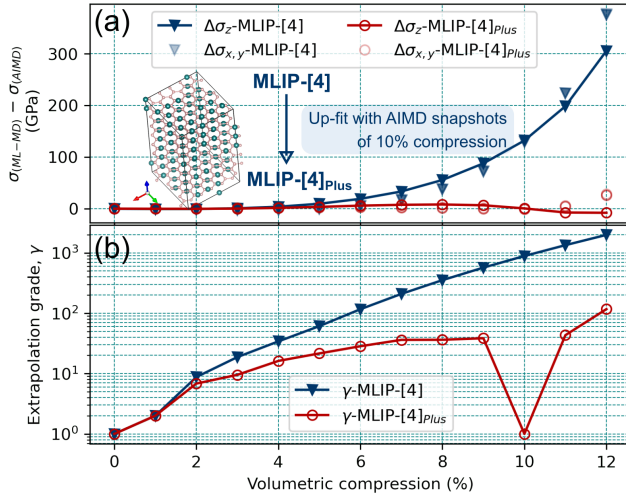


Figure 9. Transferability of the here-developed MLIP (MLIP-[4]) to atomic scale room-temperature simulations of volumetric compression. (a) Differences in main stress tensor components ($\sigma_{x,y}$, in the basal plane, and σ_z in the [0001] direction) between ML-MD and AIMD simulations, plotted as a function of the compression percentage. (b) Evolution of extrapolation grades. Blue and red data point correspond to ML-MD simulation with different MLIPs, MLIP-[4] and MLIP-[4]_{plus}.

- **Off-stoichiometric TiB₂ structures and other phases.**

Our MLIP was trained to snapshots of TiB₂ (AlB₂-type phase, P6/mmm) with a perfect stoichiometry (speaking of the entire supercell). Visualization of the training set (Fig. 3c), however, indicates presence of atomic environments with various Ti-to-B ratios as well as bond lengths and angles different from those in TiB₂. This may be useful for simulations of e.g. vacancy-containing TiB₂ structures commonly reported by synthesis³⁹ or other phases in the Ti–B phase diagram, although it is quite a stretch from the intended applicability of our MLIP.

To investigate transferability to other phases, we use MS to find the ground-state of known phases from the Ti–B phase diagram⁸⁵: Ti₂B (tetragonal, I4/mcm), Ti₃B₄ (orthorhombic, Immm), and TiB (orthorhombic Pnma) at 0 K^{xxiii}. Additionally, we equilibrate the TiB₂ phase with Ti, B, or combined Ti and B vacancies: Ti₃₆B₇₁, Ti₃₅B₇₂, and Ti₃₅B₇₀. For all calculations, extrapolation grades ($\gamma \approx 10^2$ – 10^4) are far beyond *reliable* extrapolation. In terms of total energies (E_{tot}), and lattice parameters (a , b , c), the largest deviation from *ab initio* values is exhibited by Ti₃B₄ (yielding 10% and 2.5% deviation from *ab initio* E_{tot} and c , respectively).

Simulations of other stoichiometries and phases therefore require up-fitting (not necessarily due to poor accuracy but especially due to high uncertainty, $\gamma \gg \gamma_{reliable}$). To illustrate the up-fitting effect, MLIP-[4] learns from additional *ab initio* snapshots: from 0 K equilibration of a 780-atom Ti₃B₄ supercell. Prior to up-fitting, equilibra-

^{xxiii}The supercell sizes are always ≈ 700 atoms, i.e. comparable to that used for TiB₂.

Table 4. Zero Kelvin surface energies, E_{surf} (in J/m²), of low-index TiB₂ surfaces predicted with the here-developed MLIP (MLIP-[4]), compared to reference *ab initio* values.

	Surface	E_{surf}	Source
ML-MS	(0001)	3.80	This work
DFT	(0001)	3.80	This work
DFT	(0001)	4.50–4.72	Ref. ⁸⁶
DFT	(0001)	4.22–4.24	Ref. ⁸⁷
DFT	(0001)	4.14	Ref. ⁸⁸
DFT	(0001)	≈ 4.20	Ref. ⁸⁹
ML-MS	(10 $\bar{1}$ 0)	3.98	This work
DFT	(10 $\bar{1}$ 0)	4.12	This work
DFT	(10 $\bar{1}$ 0)	4.20–4.83	Ref. ⁸⁷
DFT	(10 $\bar{1}$ 0)	≈ 4.10	Ref. ⁸⁹
ML-MS	($\bar{1}$ 2 $\bar{1}$ 0)	3.42	This work
DFT	($\bar{1}$ 2 $\bar{1}$ 0)	3.57	This work
DFT	($\bar{1}$ 2 $\bar{1}$ 0)	5.06	Ref. ⁸⁷
DFT	($\bar{1}$ 2 $\bar{1}$ 0)	≈ 4.02	Ref. ⁸⁹

tion of Ti₃B₄ yields $\gamma \geq 10^4$. Afterwards, $\gamma \leq 5 < \gamma_{reliable}$ and E_{tot} , a and c deviate from *ab initio* values by 4.18%, 0.07%, and 0.73%^{xxiv}

Conclusions

We proposed a strategy for the development of MLIPs suitable to portray intrinsic tensile strength, toughness, and fracture mechanisms of monocrystals from atomic scale ($\approx 10^3$ atoms, accessible by *ab initio* methods) to nanoscale ($\approx 10^4$ – 10^6 atoms). Training data generation, fitting, and validation procedure were illustrated using the moment tensor potential (MTP) formalism. Material-wise, TiB₂ ceramic served as a model system. The MLIP was used to simulate room-temperature uniaxial tensile deformation of TiB₂ at length scales beyond *ab initio* reach, $\approx 5^3$ nm³– 15^3 nm³.

Key findings of our work are summarized below.

Methodological: MLIP development

1. MLIPs for simulations of tensile deformation until fracture can be trained following the scheme in Fig. 1, based on snapshots from finite-temperature AIMD simulations of sequential elongation with supercells near *ab initio* size limit ($\approx 10^3$ atoms). The strategy can be generalized to other loading conditions (e.g. shearing).
2. Due to strain-induced nucleation of extended defects, a transition from atomic to nanoscale simulations—here including also more realistic computational setup (continuous deformation, Poisson’s contraction)—may require up-fitting. We propose to generate additional *ab initio*

^{xxiv}We can also compare the structures relaxed by *ab initio* calculations and MS, by calculating differences between the corresponding atomic positions. Prior to up-fitting, square root of the maximum difference (of each corresponding atom position in Ti₃B₄, 780 at.) is 6.77 Å, which decreases to 6.60 after up-fitting. For comparison, initial TiB₂ (720 at.) configuration would have maximum difference of 2.28 Å.

data by finite-temperature AIMD: imposing a large strain along one lattice vector, initializing atoms at ideal lattice sites, and equilibrating the supercell under fixed volume and shape. Again, this can be generalized to, e.g., simple shear or compression.

3. MLIPs fitted to room-temperature tensile dataset may be transferable to simulate other loading conditions; here we show examples of high-temperature tensile deformation and shear deformation (at the atomic scale). Contrarily, up-fitting is certainly required for simulations of volumetric compression, other phases and stoichiometries.

Materials science: predictions for TiB₂

1. Our calculations indicate elastic isotropy of TiB₂'s basal plane at 300 and 1200 K.
2. Mechanical properties derived from initially dislocation-free nanoscale supercells, with $\approx 10^4$ – 10^6 atoms, are directionally dependent but well saturated. At 300 K, theoretical tensile strength during [0001], [10 $\bar{1}$ 0], and [$\bar{1}$ 2 $\bar{1}$ 0] deformation reaches 51–56 GPa. It is the highest during [$\bar{1}$ 2 $\bar{1}$ 0] loading, while toughness is the highest during [0001] loading.
3. Nanoscale MD simulations provide insights into crack nucleation and growth mechanisms. Subject to [0001] tensile loading, Ti/B₂ layer delamination induces opening of nm-sized voids which rapidly coalesce, inducing formation of few-nm-size cracks inside the material. Fracture surfaces align predominantly with basal planes, {0001}, and first order pyramidal planes, {10 $\bar{1}$ 1}.
4. Considering deformation within the basal plane, [10 $\bar{1}$ 0] tensile test (i.e. loading in the direction of strong B–B bonds), most often induces crack deflection, formation of V-shaped defects, and fracture at {11 $\bar{2}$ 2} family of surfaces. Contrarily, the [$\bar{1}$ 2 $\bar{1}$ 0] tensile deformation induces fracture at {10 $\bar{1}$ 0} prismatic planes.

In projection, the here-proposed training strategy should be applicable to other ceramics (particularly transition metal diborides but also e.g. nitrides, carbides) as well as other MLIP formalisms (e.g. neural network potentials). Our nanoscale simulations for TiB₂ provide guidance for interpretation of micromechanics experiments, in particular, can complement post-mortem transmission electron microscopy. Follow-up work could focus on MLIP up-fitting for more complex loading geometries, e.g., with a pre-crack.

Methods

Ab initio molecular dynamics (AIMD)

Born-Oppenheimer AIMD calculations were carried out using the VASP⁹⁰ package together with the projector augmented wave (PAW)⁹¹ method and the Perdew-Burke-Ernzerhof exchange-correlation functional revised for solids (PBEsol)⁹². All TiB₂ supercells were based on the AlB₂-type structure (P6/mmm). The

720-atom (240 Ti+480 B) supercell—used to generate the training/learning/validation dataset—had $\approx (1.5 \times 1.6 \times 2.6)$ nm³, with x, y, z axes chosen to satisfy to following crystallographic relationships: $x \parallel [10\bar{1}0], y \parallel [\bar{1}2\bar{1}0], z \parallel [0001]$.

Equilibration of TiB₂ (at 300 and 1200 K, with Γ point only) was performed in 2 steps: (i) a 10 ps AIMD run with isobaric-isothermal (NPT) ensemble, Parrinello-Rahman barostat⁹³ and Langevin thermostat, and (ii) a 2 ps for 300 K, 4 ps for 1200 K AIMD run with the canonical (NVT) ensemble with Nosé-Hoover thermostat, using time-averaged lattice parameters from the NPT simulation (time steps with reasonably converged energy and stresses—see the Suppl. Mat., Fig. S1). Computational setup for simulations of [0001], [10 $\bar{1}$ 0], and [$\bar{1}$ 2 $\bar{1}$ 0] **tensile deformation** and (0001)[$\bar{1}$ 2 $\bar{1}$ 0], (10 $\bar{1}$ 0)[$\bar{1}$ 2 $\bar{1}$ 0], and (10 $\bar{1}$ 0)[0001] **shear deformation** (all with Γ point only) followed Refs.^{69,94,95}. Specifically, the equilibrated supercell was elongated (for shear: tilted) in the desired direction (for shear: angle) with a 2%-strain step. No shrinkage of lattice parameters due to Poisson's effect was allowed. Each deformation step consisted in an 0.3 ps pre-relaxation (isokinetic velocity rescaling) and a 2.7 ps NVT run.

Stress tensor components were calculated as averages of the last 0.5 ps. **Elastic constants**, C_{ij} , were evaluated following Ref.⁷⁵, based on a second-order polynomial fit of the [0001], [10 $\bar{1}$ 0], and [$\bar{1}$ 2 $\bar{1}$ 0] stress/strain data ($C_{11}, C_{12}, C_{13}, C_{33}$) and of the (0001)[$\bar{1}$ 2 $\bar{1}$ 0], (10 $\bar{1}$ 0)[$\bar{1}$ 2 $\bar{1}$ 0], and (10 $\bar{1}$ 0)[0001] shear stress/strain data (C_{44}), assuming strains up to 4%.

For purposes of the Transferability section, simulations of **volumetric compression** were carried out for a 720-atom TiB₂ supercell maintained at 300 K (for 2 ps) with the NVT ensemble. **Surface energies** were calculated using a 60-atom TiB₂ supercell ($2 \times 1 \times 5$, with a \mathbf{k} -mesh of 60 in each direction) together with a 10Å vacuum layer. The supercell was fully relaxed at 0 K (in terms of lattice constants and atomic positions) until forces on atoms were below 10^{-5} eV/Å and total energy was converged until 0.01 eV/supercell. Other **ground-state and higher-energy structures from the Ti–B phase diagram** (Ti₂B, Ti₃B₄, TiB, TiB₁₂, etc.) were fully relaxed at 0 K starting from lattice parameters and atomic positions from the Materials Project⁸⁵, applying the same convergence criteria as for surface energies.

Development of machine-learning interatomic potentials (MLIPs)

We used the moment tensor potential (MTP) formalism, as implemented in the MLIP-2 package⁹⁶. Training data generation and general workflow are detailed in the section Training dataset generation and workflow. Note that the pool of training/learning/validation configurations did not contain snapshots from the very initial stage (first 5%) of NVT simulations (with potentially largely oscillating total energies). MLIPs were fitted based on the 16g MTPs (referring to the highest degree of polynomial-like basis functions in the analytic description of the MTP²⁸), using the Broyden-Fletcher-Goldfarb-Shanno method⁹⁷ with 1500 iterations and 1.0, 0.01 and 0.01 weights for total energy, stresses and forces in the loss functional. The cutoff radius of 5.5 Å was employed, similar to other recent MLIP studies^{23,98} (our tests for larger cutoffs, 7.4 and 10.0 Å did not show notable changes in accuracy).

Molecular dynamics with MLIPs (ML-MD)

ML-MD calculations were performed with the LAMMPS code⁹⁹ interfaced with MLIP-2 package⁹⁶ which allows to run simulations with MTP-type potentials. Computational setup of **atomic scale ML-MD tensile and shear tests** (at 300 or 1200 K) was equivalent to

AIMD tensile and shear tests described above, in particular, carried out for TiB₂ with the same supercell size and orientation. Stress tensor components and elastic constants were calculated in the same way as described above in case of AIMD.

Nanoscale ML-MD tensile tests (at 300 or 1200 K) used TiB₂ supercells with 12,960 atoms (S1); 141,120 atoms (S2); 230,400 atoms (S3); and 432,000 atoms (S4); with dimensions of about (1.5 × 1.6 × 2.6) nm³, (4.6 × 4.7 × 5.1) nm³, (10.6 × 11.0 × 10.3) nm³, (12.1 × 12.6 × 12.9) nm³, and (15.2 × 15.8 × 15.4) nm³, respectively. Prior to simulating mechanical deformation, the supercells were equilibrated for 5 ps at the target temperature (300 or 1200 K) using the isobaric-isothermal (NPT) ensemble coupled to the Nosé-Hoover thermostat with a 1 fs time step. Tensile loading was simulated by deforming the supercell at each time step with a constant strain rate (50 Å/s), accounting for lateral contraction (Poisson's effect) via the NPT thermostat.

Atomic scale **volumetric compression** simulations used analogical setup and the same supercell sizes as described above in case of AIMD. **Surface structures and other Ti-B phases** were fully relaxed at 0 K to a local energy minimum using the conjugate gradient method (molecular statics, MS) following analogical setup as described above in case of *ab initio* calculations.

Visualization and structural analysis

The OVITO package¹⁰⁰ allowed to visualize and analyze selected AIMD and ML-MD simulations, in particular, using functions (i) *Radial pair distribution function* (with a cut-off radius of 5.5 Å, i.e. the cutoff of our potentials), (ii) *Elastic strain calculation* and (iii) *Atomic strain* (with cut-off radius of ± 0.1 mm). For details see the OVITO documentation.

References

1. Liu, Y. *et al.* Stacking fault and partial dislocation dominated strengthening mechanisms in highly textured Cu/Co multilayers. *Int. J. Plast.* **49**, 152–163 (2013).
2. Sabzi, H. E. *et al.* The effects of bimodal grain size distributions on the work hardening behavior of a transformation-twinning induced plasticity steel. *Mater. Sci. Eng. A* **678**, 23–32 (2016).
3. Yang, Y. *et al.* Impact of carbon nanotube defects on fracture mechanisms in ceramic nanocomposites. *Carbon* **115**, 402–408 (2017).
4. Khosrownejad, S. M., Kermode, J. R. & Pastewka, L. Quantitative prediction of the fracture toughness of amorphous carbon from atomic-scale simulations. *Phys. Rev. Mater.* **5**, 023602 (2021).
5. Bianchini, F., Glielmo, A., Kermode, J. & De Vita, A. Enabling QM-accurate simulation of dislocation motion in γ -Ni and α -Fe using a hybrid multiscale approach. *Phys. Rev. Mater.* **3**, 043605 (2019).
6. Zhao, Y. Understanding and design of metallic alloys guided by phase-field simulations. *npj Comput. Mater.* **9**, 94 (2023).
7. Rassoulinejad-Mousavi, S. M. & Zhang, Y. Interatomic potentials transferability for molecular simulations: A comparative study for platinum, gold and silver. *Sci. Rep.* **8**, 2424 (2018).
8. Bianchini, F., Kermode, J. & De Vita, A. Modelling defects in Ni–Al with EAM and DFT calculations. *Model. Simul. Mat. Sci. Eng.* **24**, 045012 (2016).
9. Proville, L., Rodney, D. & Marinica, M.-C. Quantum effect on thermally activated glide of dislocations. *Nat. materials* **11**, 845–849 (2012).
10. Deringer, V. L., Caro, M. A. & Csányi, G. Machine learning interatomic potentials as emerging tools for materials science. *Adv. Mater.* **31**, 1902765 (2019).
11. Zuo, Y. *et al.* Performance and cost assessment of machine learning interatomic potentials. *J. Phys. Chem. A* **124**, 731–745 (2020).
12. Podryabinkin, E. V., Tikhonov, E. V., Shapeev, A. V. & Oganov, A. R. Accelerating crystal structure prediction by machine-learning interatomic potentials with active learning. *Phys. Rev. B* **99**, 064114 (2019).
13. Kang, P.-L., Shang, C. & Liu, Z.-P. Large-scale atomic simulation via machine learning potentials constructed by global potential energy surface exploration. *Acc. Chem. Res.* **53**, 2119–2129 (2020).
14. Drautz, R. Atomic cluster expansion for accurate and transferable interatomic potentials. *Phys. Rev. B* **99**, 014104 (2019).
15. Smith, J. S., Isayev, O. & Roitberg, A. E. ANI-1: an extensible neural network potential with DFT accuracy at force field computational cost. *Chem. science* **8**, 3192–3203 (2017).
16. Shapeev, A. V., Podryabinkin, E. V., Gubaev, K., Tasnádi, F. & Abrikosov, I. A. Elinvar effect in β -Ti simulated by on-the-fly trained moment tensor potential. *New J. Phys.* **22**, 113005 (2020).
17. Nishiyama, T., Seko, A. & Tanaka, I. Application of machine learning potentials to predict grain boundary properties in fcc elemental metals. *Phys. Rev. Mater.* **4**, 123607 (2020).
18. Deng, F., Wu, H., He, R., Yang, P. & Zhong, Z. Large-scale atomistic simulation of dislocation core structure in face-centered cubic metal with Deep Potential method. *Comput. Mater. Sci.* **218**, 111941 (2023).
19. Mori, H. & Ozaki, T. Neural network atomic potential to investigate the dislocation dynamics in bcc iron. *Phys. Rev. Mater.* **4**, 040601 (2020).
20. Rosenbrock, C. W. *et al.* Machine-learned interatomic potentials for alloys and alloy phase diagrams. *npj Comput. Mater.* **7**, 24 (2021).
21. Zong, H., Pilania, G., Ding, X., Ackland, G. J. & Lookman, T. Developing an interatomic potential for martensitic phase transformations in zirconium by machine learning. *npj Comput. Mater.* **4**, 48 (2018).
22. Li, X.-G. *et al.* Quantum-accurate spectral neighbor analysis potential models for Ni–Mo binary alloys and fcc metals. *Phys. Rev. B* **98**, 094104 (2018).
23. Tasnádi, F., Bock, F., Tidholm, J., Shapeev, A. V. & Abrikosov, I. A. Efficient prediction of elastic properties of Ti_{0.5}Al_{0.5}N at elevated temperature using machine learning interatomic potential. *Thin Solid Films* **737**, 138927 (2021).
24. Thompson, A. P., Swiler, L. P., Trott, C. R., Foiles, S. M. & Tucker, G. J. Spectral neighbor analysis method for automated generation of quantum-accurate interatomic potentials. *J. Comput. Phys.* **285**, 316–330 (2015).
25. Behler, J. Atom-centered symmetry functions for constructing high-dimensional neural network potentials. *J. Chem. Phys.* **134**, 074106 (2011).

26. Behler, J. Constructing high-dimensional neural network potentials: a tutorial review. *Int. J. Quantum Chem.* **115**, 1032–1050 (2015).
27. Bartók, A. P., Payne, M. C., Kondor, R. & Csányi, G. Gaussian approximation potentials: The accuracy of quantum mechanics, without the electrons. *Phys. Rev. Lett.* **104**, 136403 (2010).
28. Shapeev, A. V. Moment tensor potentials: A class of systematically improvable interatomic potentials. *Multiscale Model. Simul.* **14**, 1153–1173 (2016).
29. Seko, A., Togo, A. & Tanaka, I. Group-theoretical high-order rotational invariants for structural representations: Application to linearized machine learning interatomic potential. *Phys. Rev. B* **99**, 214108 (2019).
30. Lysogorskiy, Y. *et al.* Performant implementation of the atomic cluster expansion (PACE) and application to copper and silicon. *npj Comput. Mater.* **7**, 1–12 (2021).
31. Qamar, M., Mrovec, M., Lysogorskiy, Y., Bochkarev, A. & Drautz, R. Atomic cluster expansion for quantum-accurate large-scale simulations of carbon. *J. Chem. Theory Comput.* **19**, 5151–5167 (2023).
32. Rowe, P., Csányi, G., Alfe, D. & Michaelides, A. Development of a machine learning potential for graphene. *Phys. Rev. B* **97**, 054303 (2018).
33. Nie, A. *et al.* Direct observation of room-temperature dislocation plasticity in diamond. *Matter* **2**, 1222–1232 (2020).
34. Sivaraman, G. *et al.* Machine-learned interatomic potentials by active learning: amorphous and liquid hafnium dioxide. *npj Comput. Mater.* **6**, 104 (2020).
35. Fiedler, L. *et al.* Predicting electronic structures at any length scale with machine learning. *npj Comput. Mater.* **9**, 115 (2023).
36. Chen, Z. *et al.* Room-temperature deformation of single crystals of ZrB₂ and TiB₂ with the hexagonal AlB₂ structure investigated by micropillar compression. *Sci. Rep.* **11**, 14265 (2021).
37. Zhang, T. *et al.* Preparation of highly-dense TiB₂ ceramic with excellent mechanical properties by spark plasma sintering using hexagonal TiB₂ plates. *Mater. Res. Express* **6**, 125055 (2019).
38. Munro, R. G. Material properties of titanium diboride. *J. Res. Natl. Institute Standards Technol.* **105**, 709 (2000).
39. Magnuson, M., Hultman, L. & Högberg, H. Review of transition-metal diboride thin films. *Vacuum* **196**, 110567 (2022).
40. Holleck, H. Material selection for hard coatings. *J. Vac. Sci. Technol.* **4**, 2661–2669 (1986).
41. Golla, B. R., Mukhopadhyay, A., Basu, B. & Thimmappa, S. K. Review on ultra-high temperature boride ceramics. *Prog. Mater. Sci.* **111**, 100651 (2020).
42. Wang, C., Akbar, S., Chen, W. & Patton, V. Electrical properties of high-temperature oxides, borides, carbides, and nitrides. *J. Mater. Sci.* **30**, 1627–1641 (1995).
43. Sevik, C., Bekaert, J., Petrov, M. & Milošević, M. V. High-temperature multigap superconductivity in two-dimensional metal borides. *Phys. Rev. Mater.* **6**, 024803 (2022).
44. Wiedemann, R., Oettel, H. & Jerez, M. Structure of deposited and annealed TiB₂ layers. *Surf. Coat. Technol.* **97**, 313–321 (1997).
45. Hofmann, W. & Jäniche, W. Die struktur von aluminiumborid AlB₂. *Zeitschrift für Physikalische Chemie* **31**, 214–222 (1936).
46. Eorgan, J. & Fern, N. Zirconium diboride coatings on tantalum. *JOM* **19**, 6–11 (1967).
47. Norton, J. T., Blumenthal, H. & Sindeband, S. Structure of diborides of titanium, zirconium, columbium, tantalum and vanadium. *JOM* **1**, 749–751 (1949).
48. Mikula, M. *et al.* Mechanical properties of superhard TiB₂ coatings prepared by DC magnetron sputtering. *Vacuum* **82**, 278–281 (2007).
49. Geng, J. *et al.* Microstructural and mechanical anisotropy of extruded in-situ TiB₂/2024 composite plate. *Mater. Sci. Eng.* **687**, 131–140 (2017).
50. Zhang, T. F., Gan, B., Park, S.-m., Wang, Q. M. & Kim, K. H. Influence of negative bias voltage and deposition temperature on microstructure and properties of superhard TiB₂ coatings deposited by high power impulse magnetron sputtering. *Surf. Coat. Technol.* **253**, 115–122 (2014).
51. Mikula, M. *et al.* Mechanical properties of superhard TiB₂ coatings prepared by dc magnetron sputtering. *Vacuum* **82**, 278–281 (2007).
52. Fuger, C. *et al.* Revisiting the origins of super-hardness in TiB_{2+z} thin films—impact of growth conditions and anisotropy. *Surf. Coat. Technol.* **446**, 128806 (2022).
53. Zhou, Y., Wang, J., Li, Z., Zhan, X. & Wang, J. First-principles investigation on the chemical bonding and intrinsic elastic properties of transition metal diborides TMB₂ (TM= Zr, Hf, Nb, Ta, and Y). *Ultra-High Temp. Ceram. Mater. for Extrem. Environ. Appl.* 60–82 (2014).
54. Dai, F.-Z. & Zhou, Y. Effects of transition metal (TM= Zr, Hf, Nb, Ta, Mo, W) elements on the shear properties of TMB₂s: A first-principles investigation. *Comput. Mater. Sci.* **117**, 266–269 (2016).
55. Zhang, X., Luo, X., Li, J., Hu, P. & Han, J. The ideal strength of transition metal diborides TMB₂ (TM= Ti, Zr, Hf): Plastic anisotropy and the role of prismatic slip. *Scripta Materialia* **62**, 625–628 (2010).
56. Attarian, S. & Xiao, S. Development of a 2NN – MEAM potential for TiB system and studies of the temperature dependence of the nanohardness of TiB₂. *Comput. Mater. Sci.* **201**, 110875 (2022).
57. Attarian, S. *Multiscale modeling of Ti/TiB composites*. Ph.D. thesis, The University of Iowa (2021).
58. Timalisina, B. *Development of Eam and Rf – MEAM Interatomic Potential for Zirconium Diboride*. Ph.D. thesis, Missouri State University (2021).
59. Daw, M. S., Lawson, J. W. & Bauschlicher Jr, C. W. Interatomic potentials for zirconium diboride and hafnium diboride. *Comput. Mater. Sci.* **50**, 2828–2835 (2011).
60. Podryabinkin, E. V. & Shapeev, A. V. Active learning of linearly parametrized interatomic potentials. *Comput. Mater. Sci.* **140**, 171–180 (2017).
61. Gubaev, K., Podryabinkin, E. V. & Shapeev, A. V. Machine learning of molecular properties: Locality and active learning. *The J. chemical physics* **148**, 241727 (2018).
62. Lysogorskiy, Y., Bochkarev, A., Mrovec, M. & Drautz, R. Active learning strategies for atomic cluster expansion models. *Phys. Rev. Mater.* **7**, 043801 (2023).

63. Podryabinkin, E., Garifullin, K., Shapeev, A. & Novikov, I. MLIP-3: Active learning on atomic environments with Moment Tensor Potentials. *arXiv preprint arXiv:2304.13144* (2023).
64. Chicco, D., Warrens, M. J. & Jurman, G. The coefficient of determination R-squared is more informative than SMAPE, MAE, MAPE, MSE and RMSE in regression analysis evaluation. *PeerJ Comput. Sci.* **7**, e623 (2021).
65. Willmott, C. J. Some comments on the evaluation of model performance. *Bull. Am. Meteorol. Soc.* **63**, 1309–1313 (1982).
66. Figueiredo Filho, D. B., Júnior, J. A. S. & Rocha, E. C. What is R2 all about? *Leviathan (São Paulo)* 60–68 (2011).
67. Cohn, D. A., Ghahramani, Z. & Jordan, M. I. Active learning with statistical models. *J. artificial intelligence research* **4**, 129–145 (1996).
68. Fan, H. & El-Awady, J. A. Molecular dynamics simulations of orientation effects during tension, compression, and bending deformations of magnesium nanocrystals. *J. Appl. Mech.* **82**, 101006 (2015).
69. Koutná, N. *et al.* Atomistic mechanisms underlying plasticity and crack growth in ceramics: a case study of AlN/TiN superlattices. *Acta Mater.* **229**, 117809 (2022).
70. Hodapp, M. & Shapeev, A. In operando active learning of interatomic interaction during large-scale simulations. *Mach. Learn. Sci. Technol.* **1**, 045005 (2020).
71. Freitas, R. & Cao, Y. Machine-learning potentials for crystal defects. *MRS Commun.* **12**, 510–520 (2022).
72. Xiang, H., Feng, Z., Li, Z. & Zhou, Y. Temperature-dependence of structural and mechanical properties of TiB₂: A first principle investigation. *J. Appl. Phys.* **117** (2015).
73. Spoor, P. *et al.* Elastic constants and crystal anisotropy of titanium diboride. *Appl. Phys. Lett.* **70**, 1959–1961 (1997).
74. Amulele, G. M. & Manghnani, M. H. Compression studies of TiB₂ using synchrotron X-ray diffraction and ultrasonic techniques. *J. Appl. Phys.* **97**, 023506 (2005).
75. Sangiovanni, D. G. *et al.* Temperature-dependent elastic properties of binary and multicomponent high-entropy refractory carbides. *Mater. & Des.* **204**, 109634 (2021).
76. Panda, K. & Chandran, K. R. Determination of elastic constants of titanium diboride (TiB₂) from first principles using flapw implementation of the density functional theory. *Comput. Mater. Sci.* **35**, 134–150 (2006).
77. Chen, L. *et al.* A facile one-step route to nanocrystalline TiB₂ powders. *Mater. Res. Bull.* **39**, 609–613 (2004).
78. Mukaida, M., Goto, T. & Hirai, T. Preferred orientation of TiB₂ plates prepared by CVD of the TiCl₄+B₂H₆ system. *J. Mater. Sci.* **26**, 6613–6617 (1991).
79. Kelesoglu, E. & Mitterer, C. Structure and properties of TiB₂ based coatings prepared by unbalanced DC magnetron sputtering. *Surf. Coat. Technol.* **98**, 1483–1489 (1998).
80. Paul, B. *et al.* Plastic deformation of single crystals of CrB₂, TiB₂ and ZrB₂ with the hexagonal AlB₂ structure. *Acta Mater.* **211**, 116857 (2021).
81. Jiao, Y., Huang, L. & Geng, L. Progress on discontinuously reinforced titanium matrix composites. *J. Alloy. Compd.* **767**, 1196–1215 (2018).
82. Dub, S. *et al.* Mechanical properties of single crystals of transition metals diborides TMB₂ (TM= Sc, Hf, Zr, Ti). experiment and theory. *J. Superhard Mater.* **39**, 308–318 (2017).
83. Lei, J. *et al.* Synthesis and high-pressure mechanical properties of superhard rhenium/tungsten diboride nanocrystals. *ACS nano* **13**, 10036–10048 (2019).
84. Leiner, T. *et al.* On energetics of allotrope transformations in transition-metal diborides via plane-by-plane shearing. *Vacuum* **215**, 112329 (2023).
85. Jain, A. *et al.* Commentary: The materials project: A materials genome approach to accelerating materials innovation. *APL materials* **1**, 011002 (2013).
86. Guan, C. & Zhu, H. Theoretical insights into the behaviors of sodium and aluminum on the cathode titanium diboride surfaces. *Comput. Mater. Sci.* **211**, 111535 (2022).
87. Sun, W., Dai, F., Xiang, H., Liu, J. & Zhou, Y. General trends in surface stability and oxygen adsorption behavior of transition metal diborides (TMB₂). *J. materials science & technology* **35**, 584–590 (2019).
88. Clayton, J. *et al.* Deformation and failure mechanics of boron carbide–titanium diboride composites at multiple scales. *Jom* **71**, 2567–2575 (2019).
89. Gan, Q. *et al.* Robust hydrophobic materials by surface modification in transition-metal diborides. *ACS Appl. Mater. & Interfaces* **13**, 58162–58169 (2021).
90. Kresse, G. & Furthmüller, J. Efficient iterative schemes for ab initio total-energy calculations using a plane-wave basis set. *Phys. Rev. B* **54**, 11169 (1996).
91. Kresse, G. & Joubert, D. From ultrasoft pseudopotentials to the projector augmented-wave method. *Phys. Rev. B* **59**, 1758–1775 (1999).
92. Perdew, J. P. *et al.* Restoring the density-gradient expansion for exchange in solids and surfaces. *Phys. Rev. Lett.* **100**, 136406 (2008).
93. Parrinello, M. & Rahman, A. Polymorphic transitions in single crystals: A new molecular dynamics method. *J. Appl. Phys.* **52**, 7182–7190 (1981).
94. Sangiovanni, D., Tasnádi, F., Johnson, L., Odén, M. & Abrikosov, I. Strength, transformation toughening, and fracture dynamics of rocksalt-structure Ti_{1-x}Al_xN (0 ≤ x ≤ 0.75) alloys. *Phys. Rev. Mater.* **4**, 033605 (2020).
95. Sangiovanni, D., Mellor, W., Harrington, T., Kaufmann, K. & Vecchio, K. Enhancing plasticity in high-entropy refractory ceramics via tailoring valence electron concentration. *Mater. Des.* **209**, 109932 (2021).
96. Novikov, I. S., Gubaev, K., Podryabinkin, E. V. & Shapeev, A. V. The MLIP package: moment tensor potentials with MPI and active learning. *Mach. learn.: sci. technol.* **2**, 025002 (2020).
97. Fletcher, R. *Practical methods of optimization* (John Wiley & Sons, 2013).
98. Erhard, L. C., Rohrer, J., Albe, K. & Deringer, V. L. A machine-learned interatomic potential for silica and its relation to empirical models. *npj Comput. Mater.* **8**, 90 (2022).
99. Thompson, A. P. *et al.* LAMMPS - a flexible simulation tool for particle-based materials modeling at the atomic, meso, and continuum scales. *Comp. Phys. Comm.* **271**, 108171 (2022).

100. Stukowski, A. Visualization and analysis of atomistic simulation data with OVITO—the open visualization tool. *Model. Simul. Mat. Sci. Eng.* **18**, 015012 (2009).

Acknowledgements

SL acknowledges xx. LCT acknowledges xx. FT acknowledges xx. LH acknowledges financial support from the Swedish Government Strategic Research Area in Materials Science on Functional Materials at Linköping University SFO-Mat-LiU No. 2009 00971. Support from Knut and Alice Wallenberg Foundation Scholar Grants KAW2016.0358 and KAW2019.0290 is also acknowledged by LH. PHM acknowledge xx. DGS gratefully acknowledges financial support from the Swedish Research Council (VR) through Grant N° VR-2021-04426 and the Competence Center Functional Nanoscale Materials (FunMat-II) (Vinnova Grant No. 2022-03071). NK acknowledges the Austrian Science Fund, FWF, (T-1308). The computations handling were enabled by resources provided by the National Academic Infrastructure for Supercomputing in Sweden (NAISS) and the Swedish National Infrastructure for Computing (SNIC) at Sigma and Tetralith Clusters partially funded by the Swedish Research Council through grant agreements no. 2022-06725 and no. 2018-05973, as well as by the Vienna Scientific Cluster (VSC) in Austria. The authors acknowledge TU Wien Bibliothek for financial support through its Open Access Funding Program.

Author contributions statement

NK conceived and designed the project; SL carried out the simulations, analyzed the data and wrote the manuscript; NK and DGS advised on the calculations and manuscript writing; LCT and FT gave constructive suggestions during the whole process and modified the manuscript; LH and PHM supported the project financially and modified the manuscript. All authors discussed the results and commented on the manuscript.

Conflicts of interest

The authors declare that they have no known competing financial interests or personal relationships that could have appeared to influence the work reported in this paper.